CHALMERS
UNIVERSITY OF TECHNOLOGY

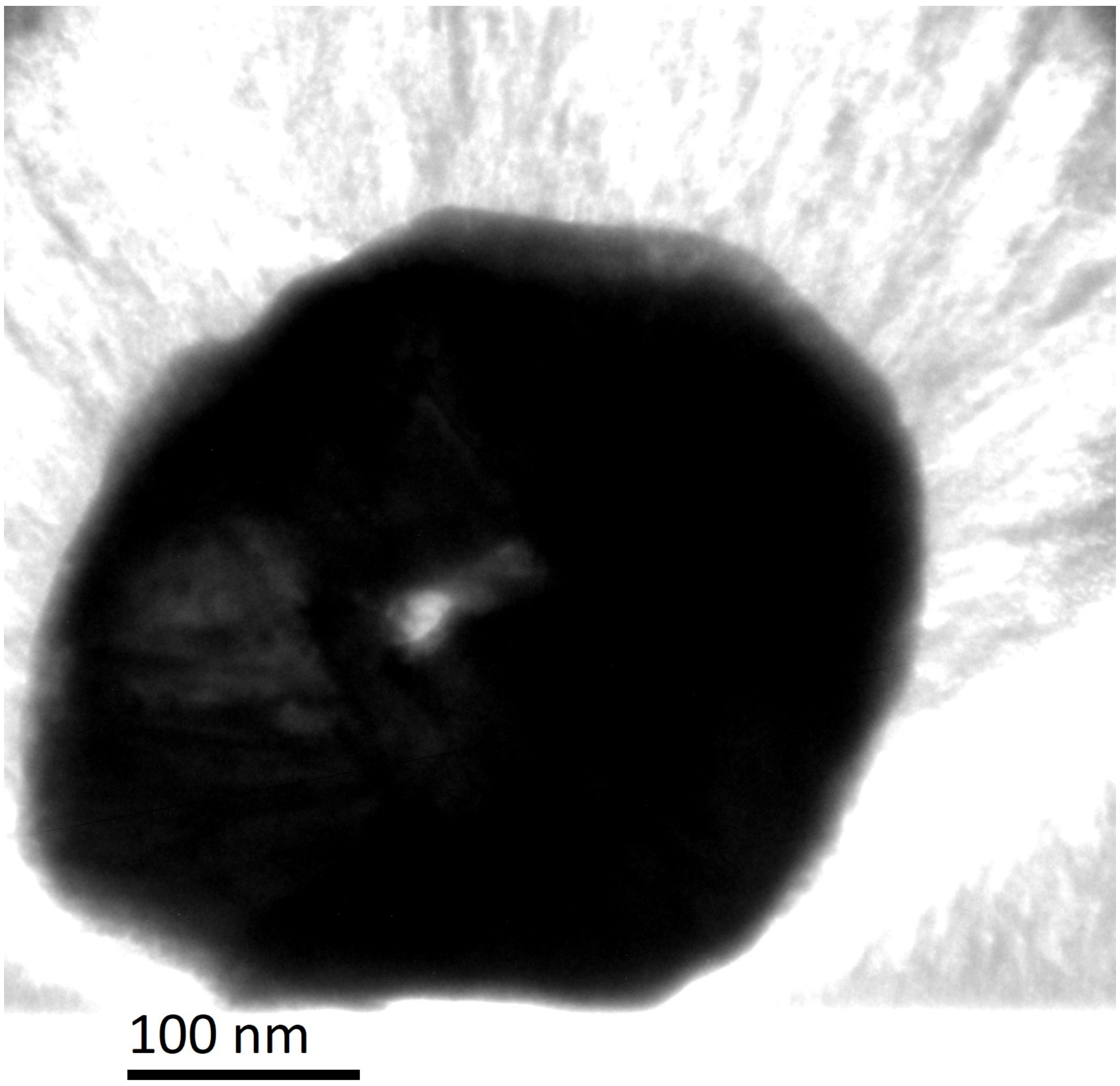

Gold-silica nanocoating of DNA origami

Towards 3D imaging biomolecules with atom probe tomography

Master's thesis in Nanotechnology

August Djuphammar

DEPARTMENT OF CHEMISTRY AND CHEMICAL ENGINEERING
Chalmers University of Technology
Gothenburg, Sweden 2022
www.chalmers.se

MASTER'S THESIS 2022

Gold-silica nanocoating of DNA origami

Towards 3D imaging biomolecules with atom probe tomography

AUGUST DJUPHAMMAR

CHALMERS
UNIVERSITY OF TECHNOLOGY

Department of Chemistry and Chemical Engineering
Division of Applied Surface Chemistry
CHALMERS UNIVERSITY OF TECHNOLOGY
Gothenburg, Sweden 2022

Gold-silica nanocoating of DNA origami
Towards 3D imaging biomolecules with atom probe tomography
AUGUST DJUPHAMMAR

Supervisor: Gustav Eriksson, Chemistry and Chemical Engineering
Examiner: Martin Andersson, Chemistry and Chemical Engineering

Master's Thesis 2022
Department of Chemistry and Chemical Engineering
Division of Applied Surface Chemistry
Chalmers University of Technology
SE-412 96 Gothenburg
Telephone +46 31 772 1000

Cover: Transmission electron microscopy image of DNA origami nanocoated with silica and gold, forming a multi-layered particle. The particle is embedded in chromium on a silicon wafer, and the sample is prepared by performing a lift-out using focused ion beam etching.

Gothenburg, Sweden 2022

Gold-silica nanocoating of DNA origami
Towards 3D imaging biomolecules with atom probe tomography
August Djuphammar
Department of Chemistry and Chemical Engineering
Chalmers University of Technology

Abstract

Finding new ways to empirically determine the 3D structure of biomolecules could greatly increase our knowledge of their function or toxicity. A long-standing issue is that biomolecules are sensitive and therefore difficult to analyze without disrupting their structure, and thereby invalidating the measurement. A promising imaging technique is atom probe tomography, which has high lateral and axial resolution, while obtaining chemical composition through mass spectrometry, yet the sensitivity issue of biomolecules remains. This Master's thesis aims to compose an atom probe tomography sample fabrication route for biomolecules, by initially stabilizing the 3D structure with nanoshells. DNA origami was folded to a distinguishable and known structure to evaluate if the nanoshell coating process affects the structure or if it is preserved. A modified Stöber process was used to form a thin silica shell around the DNA origami. This was done at mild conditions to preserve the native structure, and followed by a gold coating step, resulting in multi-layered core-shell particles. Scanning electron microscopy images and transmission electron microscopy images of the particles revealed features corresponding to the known DNA structure suggesting successful nanoshell synthesis and 3D structure preservation. What remains before atom probe tomographic analysis is possible is to form needle shaped samples with the particles at the apex, and two such paths are presented and explained as future work. The protocol could then be applied to other biomolecules with unknown structures to obtain both the chemical composition and the shape.

Keywords: DNA origami, Nanoshells, Nanoparticles, Atom probe tomography, 3D imaging, Nanobiotechnology

Acknowledgements

I would first and foremost like to thank everyone in the APT research group for all the help and the chance to pursue this thesis. Martin Andersson, my examiner, has been welcoming and enthusiastic about the project from the start and given carefully considered input throughout the project. Gustav Eriksson, my supervisor, has taught me how to operate several of the instruments used and has provided with practical help and valuable input. Mats Hulander has helped me with many practicalities in the laboratory and he has always had a genuine interest in the project and a positive attitude, resulting in several ideas and discussions. Saieesh Nayak, a fellow Master's student, has contributed in broad discussions investigating alternative solutions and completely different perspectives, due to our mutual passion for the research field and its potential. All of this has made the project possible and something I have truly enjoyed working on. I would also like to thank Jenny Perez Holmberg for kindly and cheerfully teaching me how to use and understand the analytical technique DLS, which has been of great help.

August Djuphammar, Gothenburg, June 2022

Contents

1

Introduction

Knowledge about biomolecules, like proteins and DNA, forms a basis for scientific development within life sciences. Many proteins are known in terms of their amino acid sequences, although, their 3D structures are more difficult to determine. Out of a total of 485 million known proteins [1], only 190 thousand 3D structures are determined [2], corresponding to about 0.04 %. The 3D structures of different proteins are often of high importance for their unique functions, and therefore of high interest. A long-standing issue with analyzing the 3D structure of biomolecules is that biomolecules are very sensitive. For proteins, one has to consider temperature, pH-value, and other factors which can affect denaturation [3]. Common methods where 3D information is obtained does not fulfill these criteria, meaning even if 3D information is obtained, it will not be the native 3D structure, which the protein has in the cell environment.

3D structures of proteins are historically characterized with X-ray crystallography, or for smaller proteins, with nuclear magnetic resonance [4]. These methods have limits, and the prior one is very time-consuming since the crystallization methods of proteins vary for each protein. A new trending technique is cryogenic electron microscopy, which has provided an increasing amount of protein structures each year. However, so far only the more stable proteins have been analyzed, and the yearly amount of released structures is still well below X-ray crystallography [5]. There are also computational possibilities to determine the 3D structure. Google's deep learning AI has made great progress within this field starting in 2020, where the 3D structure is estimated based on the known amino acid sequence [6]. However, any computational method has to be verified and in order to improve any AI there has to exist even more reliable data, which empirical tests can provide.

The goal of this thesis was to come further in the progress of creating new methods for 3D analysis of biomolecules. The aim is to create a sample preparation procedure which could be applied to any biomolecule, with slight modification, so that the 3D structure can be analyzed with atom probe tomography (APT). The method is based on the general idea that the 3D structure can be preserved by forming a nanoshell around the biomolecule in a gentle environment, and then being able to use more harsh analysis methods, like APT. This has been the aim for one of Martin Andersson's research groups at Chalmers University of Technology who has successfully encapsulated protein in a silica matrix previously and obtained a

3D reconstruction from APT analysis [7]. A remaining issue is that APT analysis requires samples to be shaped as sub 100nm thin needles, and the biomolecule has to be at the very apex of the tip. With their current method, the main difficulty in the fabrication of such tips is to ensure the biomolecule's position at the apex.

A possible solution is therefore to synthesize a thin silica coating around the biomolecule, followed by a thicker gold layer. The physical properties of gold are more suitable for APT analysis compared to silica, and the silica coating should preserve the 3D structure of the protein during the gold shell synthesis. The multi-layered nanoparticles are then easier to distinguish due to their size, and the high contrast of gold in various electron microscopy techniques. In order to simplify the optimization of the two-step coating protocol, DNA origami was used as the biomolecule instead of a protein. DNA is more stable and therefore an easier molecule to work with initially. DNA origami can also be tailored to obtain a specific 3D structure, making it both easier to distinguish with electron microscopy, and more suitable for verifying the method.

2

Theory

2.1 DNA origami

DNA origami is a bottom-up nanotechnology method where DNA is folded in solution in a controlled manner [8]. Usually, circular single stranded DNA, often 7 249 nucleotides long, is used as a scaffold. Various smaller single stranded DNA strands, called staple strands, are then designed in order selectively bind to specific sites on the scaffold DNA, forcing the scaffold DNA to fold [9]. To initiate the folding, the temperature is increased to the boiling point of the mixture, followed by gradual cooling. The thermal annealing disrupts the secondary DNA structures, allowing for new structures to form, causing folding of the DNA origami [10]. Today, there are software available to design the staple strands based on a desired final folded structure [11], making it a versatile tool for nanofabrication. A common purification protocol is to first add poly(ethylene glycol), PEG, then precipitate the DNA origami by centrifuging, remove the supernatant, and dissolve the DNA origami pellet. The PEG acts as a crowding agent, inhibiting excess staple strands to precipitate, and thereby separating the folded structures from excess reagents [12].

2.2 Stöber process

A commonly used method for synthesis of monodisperse silica nanoparticles was published in 1968 by Werner Stöber [13]. This method has been modified since then to fit specific applications [14, 15]. Some reoccurring precursor silicates are shown in Figure 2.1, where the left precursor is one of the precursors that Stöber originally used, and the right has been used for the functionalization in various modified Stöber methods. In the original Stöber synthesis, alkyl silicates are hydrolyzed and the resulting silicic acid undergoes condensation, thereby growing silicon dioxide [13]. An example reaction formula is presented in Equation 2.1, based on the alkyl silicate shown in Figure 2.1a.

$$\begin{gathered} Si(OEt)_4 + 4H_2O \rightleftharpoons Si(OH)_4 + 4EtOH \\ 2Si(OH)_4 \rightarrow (OH)_3Si\text{–}O\text{–}Si(OH)_3 + H_2O \end{gathered} \tag{2.1}$$

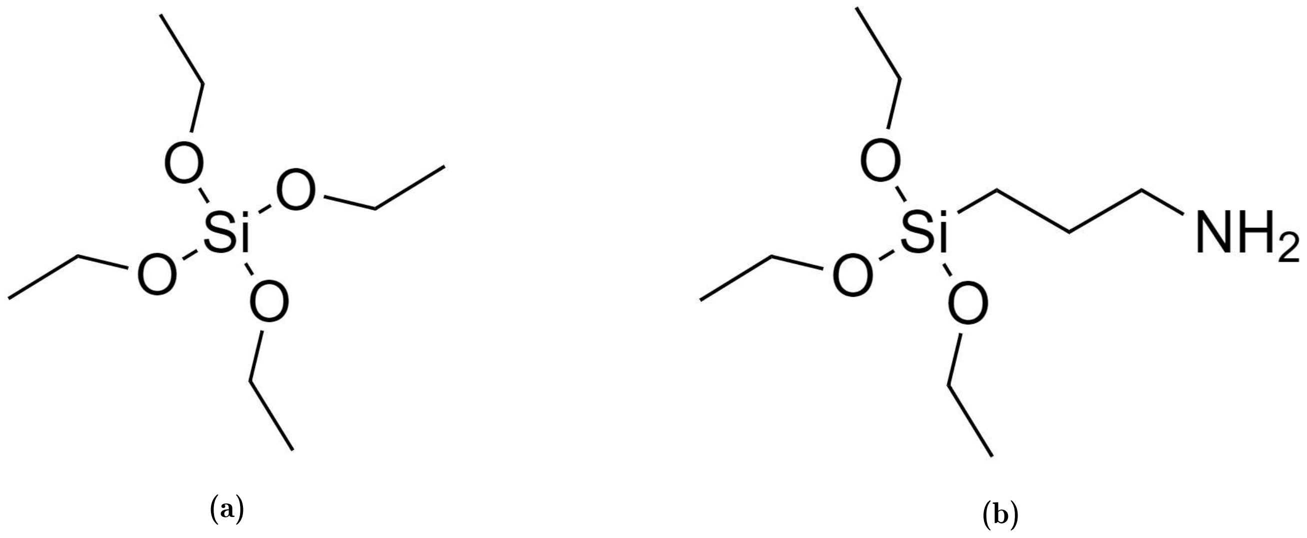

Figure 2.1: Silicates used in the Stöber and modified Stöber methods. a) Tetraethyl orthosilicate, TEOS. b) (3-Aminopropyl)triethoxysilane, APTES.

The salt concentration and the pH-value affects the resulting silica structure. The formation of 3D gel networks is promoted by the presence of salt and by lowering the pH below 7. At higher pH conditions, pH 7-10, and low salt concentration, <0.2 N, individual nanoparticles are likely to form [16].

2.3 Gold nanoshells

Gold nanoshells are particles which often are used to tailor for a specific light absorbance maximum. These consist of a gold shell surrounding a dielectric core. One common dielectric core is silica. In order to grow the gold shell on the silica particles, they are first surface modified. This is commonly performed by adding APTES, resulting in the amine group facing out in solution [17], see Figure 2.1b.

Small gold nanoparticles, $< 10nm$, are then synthesized and mixed with the surface modified silica particles, which are significantly larger. This results in adsorption of the small gold nanoparticles all around the silica particle surface. The gold nanoparticles are then grown larger by the addition of a gold salt, making them fuse into each other, and form a gold shell [18]. Both the synthesis and the growth of the gold nanoparticles are redox reactions where a gold salt, typically $HAuCl_4$, is reduced by the introduction of a reducing agent.

As the ratio between the silica core diameter and the gold shell thickness increases, the absorbance peak shifts towards longer wavelengths of light [17]. This results in a blue-shift of the absorbance peak as the gold shell grows on a fixed size silica particle. Therefore, by measuring the peak wavelength of a gold nanoshell particle with a known silica core size, the shell thickness can be determined.

2.4 Nanoparticle stability

Colloidal nanoparticles are often stabilized to avoid aggregation. There are numerous ways to enhance stability, such as introducing ligands for steric stabilization, or to promote surface charge of the particles which increase particle-particle repulsion [19]. There are also many ways to decrease stability, which in most cases should be avoided. For silica particles, the introduction of salts can induce aggregation as the surface charge repulsion becomes weakened. Divalent cations, such as Mg^{2+}, are the most effective in screening the charge repulsion. However, in deionized water, silica nanoparticles are stable in a wide range of pH, at least 2.5-10 [20]. A well known protocol for gold nanoparticle synthesis involves trisodium citrate, which acts as a reducing agent and stabilizing agent [21], and therefore, gold nanoparticles are commonly stabilized using the citrate anion.

2.5 Base piranha cleaning

A common chemical cleaning procedure in laboratories involves using base piranha solution. The base piranha solution consists of H_2O, NH_4OH and H_2O_2, often mixed in a 5:1:1 ratio. The object that needs cleaning is then immersed in, or filled with, base piranha solution and heated to 75 °C. This will cause bubbles to form, as a consequence of residues being removed. The cleaning procedure is finished once no bubbles remain [22].

2.6 UV/Vis spectroscopy

UV/Vis spectroscopy is an absorption spectroscopy technique in the ultraviolet and visible light spectrum. The absorption peak wavelength can be used to characterize the sample, and the absorbance intensity to calculate the concentration, provided that the sample absorbs within the spectrum and that the molar absorptivity is known [23]. Concentration determination of DNA is often performed by measuring the absorbance at 260 nm, correlating with the concentration of nucleotides. Proteins absorb at 280 nm, and the ratio between A260/A280 is therefore used as a DNA purity measure. A common instrument for DNA concentration analysis is the Nanodrop™, as only 1 µl is required and no cuvette is used. The software also performs the DNA concentration calculations [24].

2.7 Scanning electron microscopy

Scanning electron microscopy, SEM, is an imaging technique with high lateral resolution. The electron beam is raster scanned over a specimen with the use of electromagnetic lenses, and the intensity of a chosen outgoing signal is detected in each position, which gives rise to the relative contrast in the SEM image. Several types of interactions occur between the electrons and the specimen, and the outgoing signals can be detected using various detectors. Some of the most important interactions are the generation of secondary electrons and characteristic x-rays. Secondary electrons are generated as a consequence of ionization by the electron beam, and the amount of generated electrons is highly governed by the surface topography. The energy of secondary electrons is also low, resulting in that only the secondary electrons generated close to the sample surface can escape from the substrate. This results in higher spatial resolution, and secondary electron detection is therefore often used for topographic imaging. Characteristic x-rays can instead be detected to identify the composition of elements. The x-rays are generated once the electron beam ionizes inner shell electrons, resulting in de-excitation of higher energy electrons, followed by radiation of photons with wavelengths corresponding to the energy level difference. The energy level difference is dependant on the element, which is why it is called characteristic x-rays. The spatial resolution is significantly lower, as characteristic x-rays can escape from the substrate more easily. Therefore, it is usually only used to analyze certain positions, and not used for imaging [25]. During any imaging in the SEM, the electron beam can damage sensitive specimen, such as polymers and most organics. The damaging from the electron beam also applies to transmission electron microscopy [26].

2.8 Transmission electron microscopy

Transmission electron microscopy, TEM, is a more sophisticated electron microscopy technique compared to SEM, offering higher resolution, but often requires more sample preparation. In TEM, the substrate has to be sufficiently thin in order for the electron beam to pass through it, as the detector is on the other side. The electron acceleration voltage is also significantly higher compared to SEM for this reason. The maximum sample thickness depends on the average atomic number of the sample, as higher atomic numbers scatter electrons more. The contrast in TEM images depends on scattering, and therefore on the sample thickness and atomic composition. Depending on if the direct or diffracted electrons are collected for imaging, a bright or dark field image will be obtained, respectively. TEM grids are commonly used to image particles, which often consist of an electron transparent film mechanically supported by a more rigid grid. The specimen is then deposited on the film, for example by immersing the grid into a dispersion of the specimen. Another sample preparation technique is to perform a lift-out. In that case the specimen is deposited on a wafer, and a thin slice of the wafer in cross-section is removed and placed on a TEM lift-out holder. The lift-out itself is often performed in a focused ion beam instrument [26].

2.9 Focused ion beam

A focused ion beam, FIB, is a lithography instrument for etching small features. The etching is performed by directing a beam of heavy ions, typically gallium, at high energies towards the sample surface. It is also possible to deposit thin films [27] by injecting a precursor gas, which reacts with the ion beam [28]. In the FIB, the sample can be monitored as secondary ions are produced during the etching. Since the etching process is destructive, some FIB instruments have a complementary, integrated SEM system for non-destructive imaging [29].

2.10 Atom probe tomography

Atom probe tomography, APT, is a technique for 3D mass spectrometry imaging nano-scale volumes. The spatial resolution is less than one nanometer and the mass resolution is typically high enough to distinguish different isotopes [30]. The samples have to be shaped as needles, with an apex diameter around 50 nanometers [31]. Common methods for fabrication of the sample tips are by electropolishing and focused ion beam etching [32].

The basis of analysis is that the sample tip is subjected to a high electric field. Then, by either applying an electric pulse, or directing a laser pulse to the apex of the tip, the top atomic layer is removed atom by atom through field evaporation and the generated ions are accelerated by the electric field towards a detector. The detector then obtains spatial information based on where on the detector the ions are detected, and mass information based on the time of flight [33]. The next layer is then analyzed, either at a constant temperature by increasing the electric field, or in a constant electric field by increasing the temperature. When all atomic layers of interest have been analyzed, the obtained information is used to make a 3D reconstruction [34].

3

Methods

3.1 Materials

The water used in all experiments was freshly tapped from a Milli-Q Academic water purification system from Millipore. All other chemicals were purchased and are listed in Table 3.1. If another concentration was used than the stock concentration, it is mentioned in the running text. The theoretical structure of the folded DNA origami, which components were purchased from Tilibit Nanosystems GmbH, is shown in Figure 3.1.

Table 3.1: Chemicals, corresponding manufacturers and stock solution concentration or powder purity.

Name	**Manufacturer**	**Full description**
Acetic acid	Sigma-Aldrich	Acetic acid $\geq$99.7 %
Ammonia	Merck	Ammonia 32 %
APTES	Sigma-Aldrich	(3-Aminopropyl)triethoxysilane 99 %
EDTA	Sigma-Aldrich	Ethylenediaminetetraacetic acid 99 %
Ethanol	Solveco	Ethanol 99.5 %
Formaldehyde	Sigma-Aldrich	Formaldehyde 37 % in H_2O & 10-15 % CH_3OH
H_2O_2	Fisher	Hydrogen peroxide >30 %
$HAuCl_4$	Sigma-Aldrich	Gold(III) chloride trihydrate $\geq$99.9 %
IPA	Sigma-Aldrich	2-propanol $\geq$99.5 %
K_2CO_3	Merck	Potassium carbonate 99.995 %
MgAc	Sigma-Aldrich	Magnesium acetate $\sim$1 M in H_2O
$MgCl_2$	Sigma-Aldrich	Magnesium chloride hexahydrate 99.0-102.0 %
$NaBH_4$	Sigma-Aldrich	Sodium borohydride 99 %
NaCl	Merck	Sodium chloride $\geq$99.5 %
NaOH	Supelco	Sodium hydroxide, high purity pellets
PEG 8000	Fluka	Polyethylene glycol 8000, high purity flakes
Sodium citrate	Sigma-Aldrich	Sodium citrate tribasic dihydrate $\geq$99.0 %
TEOS	Sigma-Aldrich	Tetraethyl orthosilicate $\geq$99.0 %
Tris	Sigma-Aldrich	Tris(hydroxymethyl)aminomethane $\geq$99.8 %

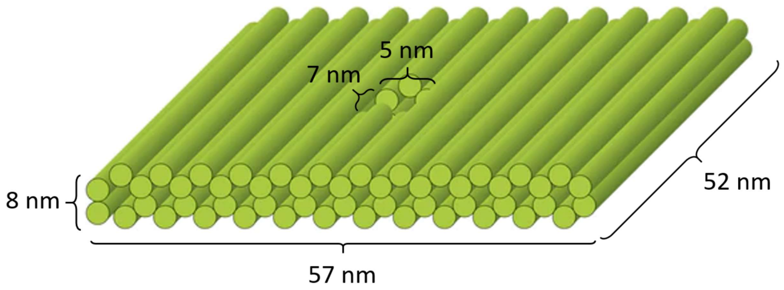

Source: Tilibit nanosystems. Reprinted and modified with permission.

Figure 3.1: Illustration of the folded DNA origami structure used.

3.2 DNA origami folding

A prefabricated DNA origami folding kit was purchased from Tilibit Nanosystems GmbH and stored at -18 °C. The chosen shape was a cuboid with a small aperture in the center, since this shape is uncommon in nature and therefore more easily distinguishable with electron microscopy. A set of various folding buffers was tested initially and compared by folding yield. The yield was obtained by measuring the DNA concentration with UV/Vis before and after the folding reaction. A folding buffer of 15 mM MgAc in H_2O was shown to give the highest yield. All subsequent folding reactions were conducted by mixing 40 µl of 15 mM MgAc in H_2O, with 20 µl of 100 nM single stranded scaffold DNA consisting of 7249 nucleobases in buffer containing 10 mM tris and 1 mM EDTA. The mixing was done in a PCR clean Eppendorf tube of model 3810X previously rinsed in H_2O and blow dried with N_2. 40 µl of single stranded staple DNA mixture containing 475 nM of each staple was then added, resulting in a ten times molar excess of staple strands. Both the scaffold DNA and staple strand DNA were thawed and let equilibrate before usage and then again stored at -18 °C. The sample was then thermally annealed from 95 °C to 20 °C at a rate of 1 °C per minute using an Eppendorf ThermoMixer C.

The folded DNA origami was purified from the excess staple strands by first adding 1:1 v/v of 18 % w/v PEG 8000 in 10 mM tris, 1 mM EDTA and 500 mM NaCl and mixing well. The sample was centrifuged at 17 000 g for 25 min and the supernatant was removed, leaving a small transparent precipitate mainly containing folded DNA origami and PEG 8000. The centrifuge was of model Micro star 17 from VWR, and was also used for all coming centrifugations. The precipitate was resuspended in 40 µl buffer containing 10 mM tris, 1 mM EDTA and 20 mM $MgCl_2$. The suspension was then purified again two times with the same method, starting by adding 1:1 v/v of PEG 8000. After the third wash, the precipitate was instead resuspended in 100 µl of 15 mM MgAc. The DNA concentration was then determined using UV/Vis, and is expected to be below the theoretical value of 20 nM corresponding to 100 % folding yield and 100 % purification yield. The final suspension was stored at 4 °C.

3.3 Silica coating

The folded DNA origami structure was coated in silica in a two step process using a modified Stöber process developed by a research group at Aalto University [14]. The primary silica coating step was performed at more gentle conditions to preserve the 3D structure of the DNA origami, and the conditions during the secondary silica coating step were set to increase shell growth kinetics as the primary shell stabilizes the structure.

3.3.1 Primary silica coating

20 µl of purified DNA origami was mixed with 2.4 µl freshly diluted APTES in 15 mM MgAc. The concentration of APTES was adapted such that the molar ratio between APTES molecules and DNA phosphate groups was 3:1. The mixture was shaken at 500 rpm for 1 h at 20 °C using an Eppendorf ThermoMixer C. The same instrument was used for all coming shaking steps. 2.8 µl of freshly diluted TEOS in 15 mM MgAc was added, with a molar ratio between TEOS molecules and DNA phosphate groups of 20:1. The pH was then adjusted to 9 by adding 50 mM NaOH. The required volume of NaOH was determined by measuring the pH of a 100 times larger volume replicate without DNA origami using a Jenway 3510 pH meter. The mixture was then shaken at 500 rpm for 5 days at 20 °C. Purification of the primary coated particles was performed by washing two times, where one wash included adding 450 µl H_2O and centrifuging at 8 000 g for 3 min, using Amicon Ultra-0.5 mL filters with a 100 kDa molecular weight cut-off. The volume of the purified remains was measured and stored at 4 °C.

3.3.2 Secondary silica coating

1 µl of purified primary silica coated DNA origami was diluted in 20 % v/v IPA in H_2O. The diluent volume was calculated based on a final concentration of DNA of 25 pM, after subsequent addition of ammonia and TEOS, provided a 100 % DNA yield during the primary coating process. The pH was then adjusted to 10.8 by adding a calculated volume of 28 % w/w ammonia, corresponding 12.6 % of the final volume. 1 µl of freshly diluted TEOS in IPA was then added, with a molar ratio between TEOS molecules and DNA phosphate groups of 5:1 provided 100 % DNA yield during the primary coating process. Next, the mixture was shaken at 500 rpm for 1 day at 20 °C. The secondary silica coated particles were washed two times using the same method as for the primary coated particles. The purified remains were then diluted in H_2O to a total of 50 µl and stored at 4 °C.

3.4 Gold coating

The gold coating procedure was based on gold nanoshell synthesis, where the silica coated DNA origami acts as the dielectric core.

3.4.1 APTES functionalization

20.4 µl of secondary silica coated DNA origami was mixed with 140 µl of freshly diluted APTES in H_2O. The APTES concentration was based on a molar ratio of 33:1 between the previously added TEOS and APTES during silica coating steps, and the newly added APTES. This was shaken at 500 rpm for 5 min at 20 °C, followed by two wash steps using Amicon Ultra-0.5 mL filters with the same method as for purifying the primary and secondary silica coated particles. The purified remains were diluted in H_2O to a total of 64 µl.

3.4.2 Synthesis of gold nanoparticles

100 ml of H_2O was stirred in a base piranha cleaned Erlenmeyer flask. 588.6 µl of 50 mM $HAuCl_4$ was added, followed by 2.72 ml of 25 mM sodium citrate. 1 ml of freshly made 0.075 % w/v $NaBH_4$ in 1 % w/v sodium citrate in H_2O was then added and stirred for ten minutes. The gold nanoparticle solution was then stored at 4 °C.

3.4.3 Gold nanoparticles surface adsorption

8 µl of the gold nanoparticle solution was diluted 200 times in H_2O, to a total of 400 µl. 58.34 µl of the APTES functionalized silica coated DNA origami solution was added and shaken at 500 rpm for 5 minutes at 20 °C, after which it was let sit for two hours. Next, the sample solution was washed three times by alternating centrifugation with the removal of 450 µl supernatant and the addition of 450 µl H_2O. The centrifugation was done at 12 000 g for 8 min to precipitate the silica coated DNA origami particles with gold nanoparticles adsorbed at the surface (GNP@SiO_2@DNA), resulting in a small transparent pellet. After the third wash, the pellet was dispersed in 83 µl H_2O by ultrasonication for one hour using an ultrasonic cleaning bath from VWR of model USC900D at the highest intensity level (9).

3.4.4 Gold shell growth

100 ml of 2 mM K_2CO_3 was stirred with 1.5 ml of 1 % w/v $HAuCl_4$ in H_2O for 30 min and left still over night at room temperature, protected from sunlight promoting gold hydroxide formation. 833 µl of the gold hydroxide solution was then shaken at 500 rpm at 20 °C, and 41.6 µl of GNP@SiO_2@DNA solution added rapidly and shaken for 5 min. Afterwards, 41.6 µl of 37 % w/w formaldehyde in H_2O was added rapidly, and shaken for 10 more minutes. The mixture was then let sit overnight after which the gold-silica coated DNA origami particles (Au@SiO_2@DNA) were washed three times. The washing was performed by alternating centrifuging at 8 000 g for 2 min with removing 450 µl supernatant and adding 450 µl H_2O. After the third wash, the pellet was dispersed in 83 µl H_2O. Some replicates were also washed a fourth time at 1 500 g for 1 min.

3.5 Characterization

The Au@SiO$_2$@DNA particles as well as some intermediate states were analyzed using UV/Vis spectroscopy, SEM and TEM. Dynamic light scattering was also used, although this method was shown unable to detect the particles due to too low concentrations, and is therefore not discussed further.

3.5.1 UV/Vis spectroscopy

DNA concentration was determined using a built-in function in the NanoDrop One^C spectrophotometer for double stranded DNA. Particles containing gold were also analyzed using a custom setting, showing the entire spectrum without performing any calculations, in order to detect any surface plasmon resonance absorption peaks. All measurements were blanked by measuring pure solvent, which the software uses for baseline correction, and conducted by adding 2 µl of sample to the lower pedestal of the instrument.

3.5.2 Scanning electron microscopy

Silicon wafers were thoroughly cleaned before usage by ultrasonic cleaning in IPA for 20 min, rinsing with 99.5 % ethanol, ultrasonic cleaning in 99.5 % ethanol for 20 min, and rinsing in H_2O. The ultrasonic cleaning was performed in an ultrasonic cleaning bath from VWR of model USC900D at the highest intensity level (9). Afterwards, the wafers were blown dry with N_2, exposed to UV/ozone in a UV/ozone cleaner for 1 h, and lastly base piranha cleaned. All the used equipment, such as tweezers and laboratory glassware, were also base piranha cleaned before handling the wafers.

5 or 10 µl of sample solution was ejected in the center of a cleaned wafer and let dry overnight in a dust free but ventilated container. The wafer was then mounted on an SEM stub of aluminium with carbon tape, both purchased from Ted Pella, Inc. All SEM images were taken using an SEM of model Ultra 55 FEG from Zeiss, operating at 2-15 kV, and using the secondary electron in-lens detector. Element characterization was performed through EDX measurements in the same instrument. The only exception is the SEM images shown in Appendix A.6, Figure A.10, which were taken using a JSM 7800F Prime from JEOL.

3.5.3 Focused ion beam etching

The FIB used was of model Versa 3D LoVac from FEI, and used to perform a lift-out for further TEM analysis. 5 µl of Au@SiO$_2$@DNA particles washed in H_2O a fourth time at 1 500 g for 1 min was let dry on a silicon wafer, previously cleaned as described in section 3.5.2. The wafer was mounted on an SEM stub and sputter coated with a 150 nm thin layer of chromium, using a sputter of model EM ACE600 from Leica. Deposition of platinum was then performed in the FIB over an area of 15x1.5 µm with high lateral density of particles, believed to be Au@SiO$_2$@DNA particles. Trenches were then milled along the long sides and one of the short sides of the area, see Figure 3.2a. The sample was then tilted and milled loose everywhere except at the top of the other short side, see Figure 3.2b. A larger area next to the short side which had been cut free was then milled in order to insert a probe in close proximity. The probe was then inserted and welded to the lift-out by platinum deposition. The other short side was then cut loose by gallium ion etching, and the probe could be ejected, see Figure 3.2c.

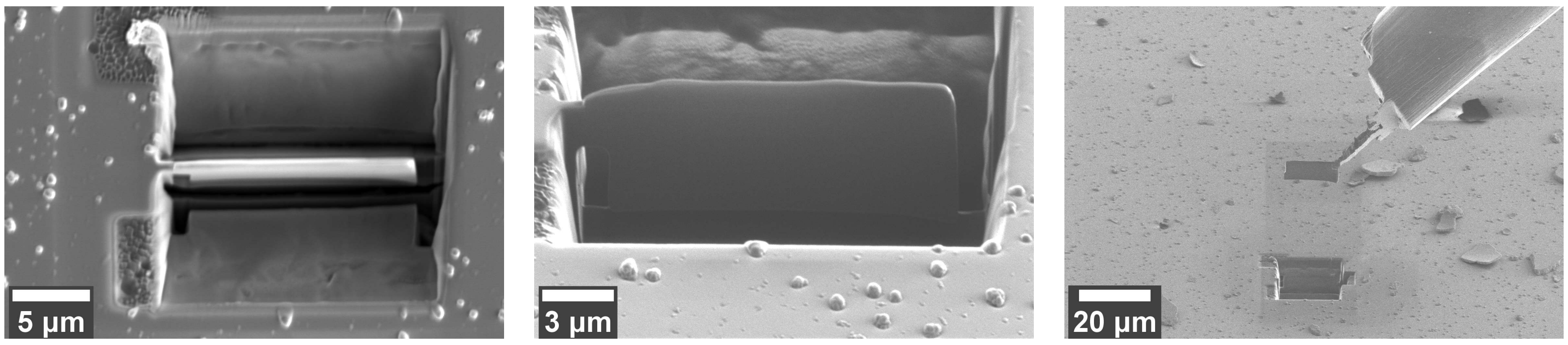

(a) (b) (c)

Figure 3.2: Secondary electron images of the lift-out process. a) SEM image of initial etching with the lift-out in the center. b) SEM image of the lift-out etched free from the bottom, viewed from 52°. c) Lift-out being ejected from the sample surface. The secondary ions forming the image are generated by the gallium ion beam.

3.5.4 Transmission electron microscopy

The Au@SiO$_2$@DNA lift-out was imaged using a Tecnai T20 LaB6 TEM from FEI. The lift-out was welded to a TEM lift-out grid from Omniprobe using platinum deposition in the FIB. After the lift-out was mounted on the grid, it was etched thinner with the ion beam, shifting towards lower ion beam current once approaching a sufficiently thin sample for TEM analysis. The grid was then stored in a dust free container, and analyzed in the TEM. All images were taken with the bright field aperture, filtering out diffracted electrons. The initial diameters and the diameters in the cross-section lift-out were measured and compared for all observed particles, as this indicates if the cross-section is at the center of the particle or towards the edge. The sputtered chromium layer was included in the diameter measurements, as the diameter of the gold only is distinguishable in the TEM images and not the SEM images in the FIB before platinum sputtering.

4

Results and Discussion

4.1 DNA origami folding

Six different solvents were investigated as folding buffer, in addition to what the pure staple and scaffold DNA were dissolved in. The tests showed the highest folded DNA origami yield with 15 mM MgAc as folding buffer, based on UV/Vis DNA concentration measurements. The final concentration after PEG purification was 10.9 nM based on the UV/Vis measurements, corresponding to a 55 % yield from the folding reaction and purification steps. Calculations and UV/Vis graphs regarding the different buffers are shown in Appendix A.1.

4.2 Silica coated DNA origami

UV/Vis measurements of the primary coated DNA origami showed a DNA concentration of 0.8 nM, although, the silica coating could have an effect on the UV/Vis absorption, decreasing the precision and reliability of the measurement. After the secondary silica coating no DNA could be measured, which is expected even if DNA is present, as the DNA concentration is heavily decreased prior to the secondary coating synthesis. The UV/Vis spectra are shown in Appendix A.2. The secondary silica coated particles were also imaged with SEM. Figure 4.1 shows images of the surface with increasing magnification from subfigure a to c. The relatively large particles sizes and clustering of particles makes it difficult to determine if the particle cores contain DNA origami. Further away from the silica cluster sheets, individual particles were found. Some of these are presented in Figure 4.2. The increase in brightness in the center and at the edges could be due to an edge effect, meaning that the center is hollow, suggesting that it is SiO_2@DNA particles based on the DNA origami structure, shown in Figure 3.1. In Figure 4.2c, which is a rotated and magnified version of Figure 4.2b, the green rectangle represents the theoretical size of the DNA origami structure lying in the imaging plane. However, if the DNA would be tilted with regards to the surface, the side lengths would decrease. The great fit to the theoretical size, and the contrast differences, therefore suggest that the folding and silica coating was successful for the imaged particle. It also indicates that the assumption that the silica coating procedure preserves the native structure is true. The particle also vanished over time during imaging, as a consequence of the electron scanning. The sensitivity of the particle indicates that it is partly organic, as no pure silica particles of the same size showed the same phenomenon. It also explains the difficulty of finding the particles with SEM, as the electron beam has to be well aligned and focused in order to image at the required magnification, which is adjusted while imaging, and therefore while destroying the particle.

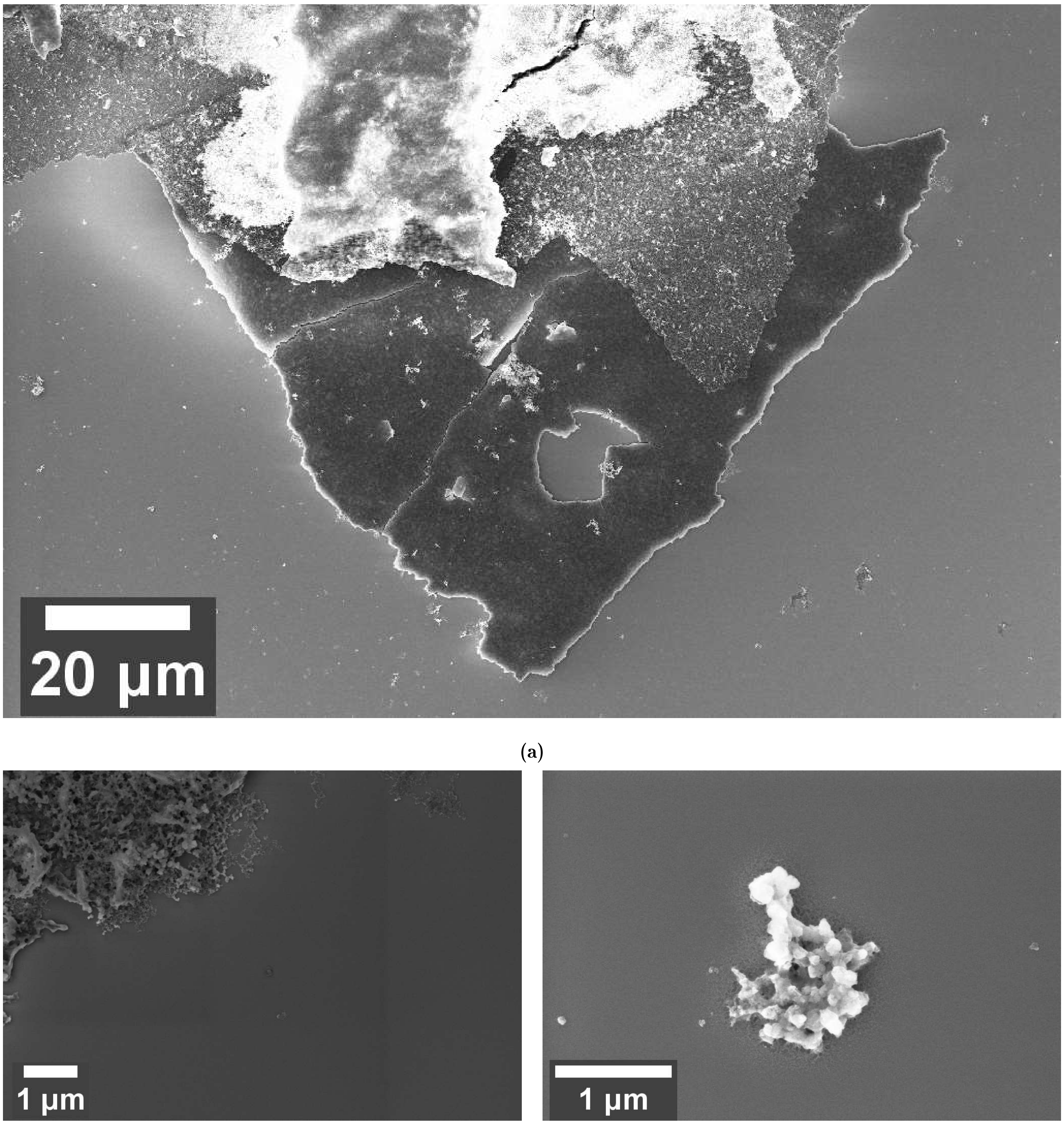

(a)

(b)

(c)

Figure 4.1: Silica clusters at increasing magnification from a to c. a) Sheets of silica clusters. b) Edge of one silica cluster sheet. c) Smaller silica cluster.

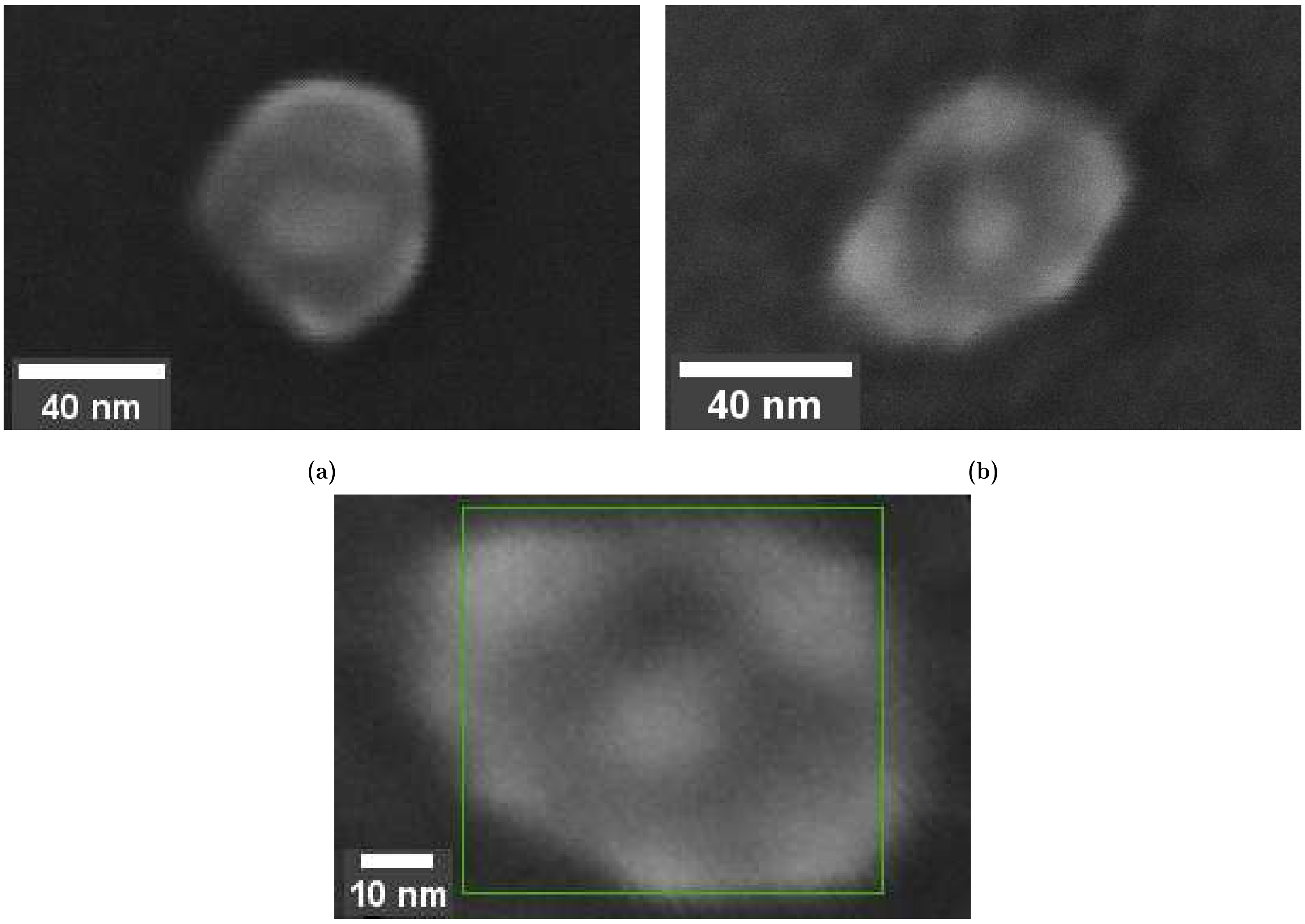

(a) (b)

(c)

Figure 4.2: a, b) Particles which are brighter in the center. c) Enlarged and rotated version of Figure 4.2b. The green rectangle shows the theoretical size of a DNA origami structure in the plane orthogonal to the viewing angle, corresponding to 57x52 nm.

4.3 Gold-silica coated DNA origami

After the gold coating the clustered regions remained, now with brighter particles spread out over the clusters. In Figure 4.3a an overview of a cluster is seen. The average diameter of the brighter particles is 395±22 nm, based on a total of 152 measurements of 19 particles. Each particle diameter was measured in 8 directions, with a shift of about 22.5° between each direction. A magnified image of four particles can be seen in Figure 4.3b. An image was also taken of small gold nuclei on the background network structure, see Figure 4.3c. The small bright particles, <10nm in diameter, seen only at the surface of the two brighter regions are expected to be the small gold nanoparticles used for the gold shell growth, due to the accurate size and higher brightness. This suggests that the background network structure is not made of gold, and is therefore most likely a silica gel. An explanation for why not these small gold nanoparticles have grown larger could be that the network surrounded the gold nanoparticles in the growth solution and thereby limited the growth possibility. This would further suggest that the SiO_2@DNA particles were separated from the network structures while in solution, since the gold shell could grow freely around them. The incorporation of the Au@SiO$_2$@DNA particles into the network structure might therefore occur during the drying of the solution onto the silicon wafer.

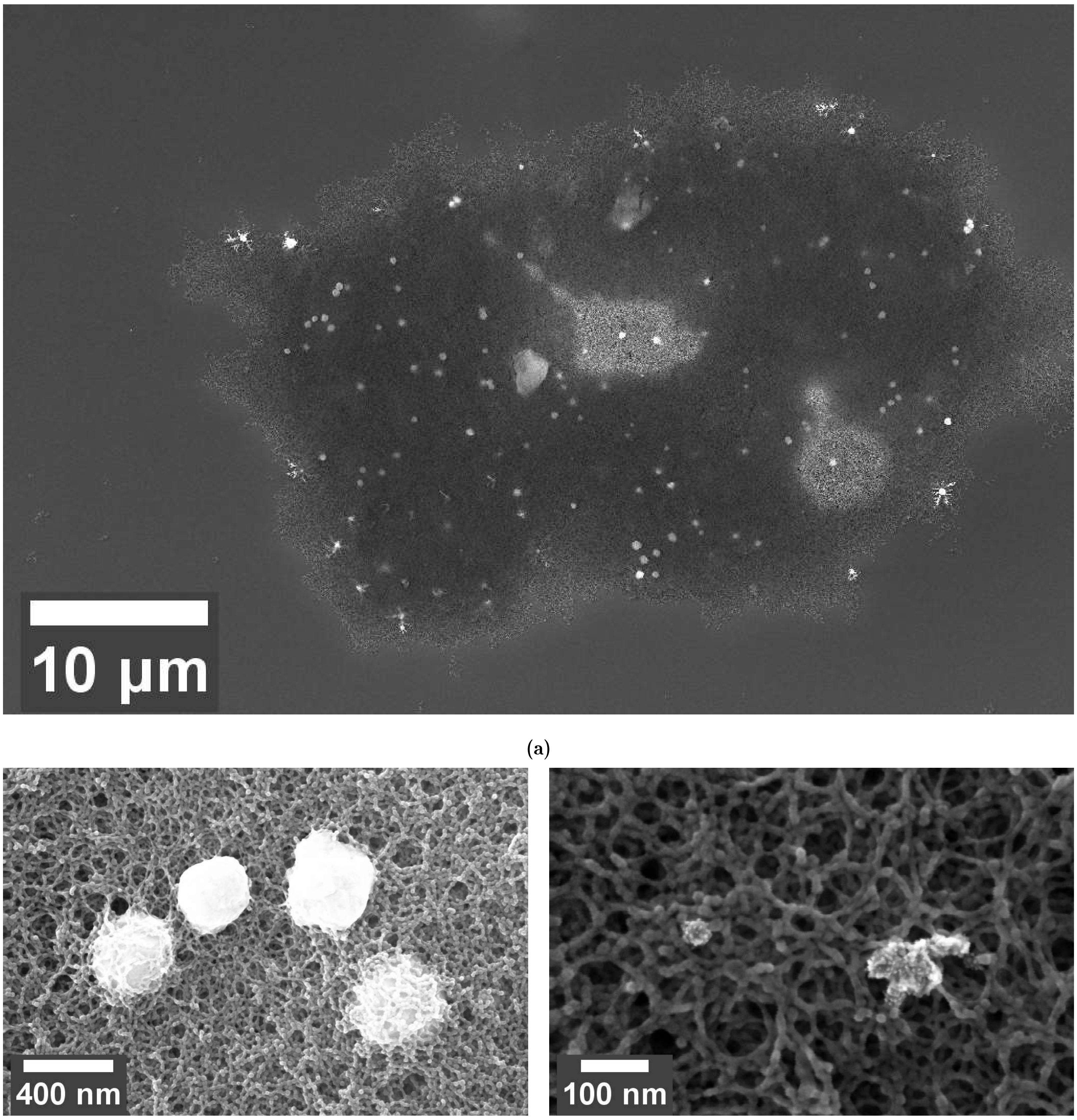

(a)

(b)

(c)

Figure 4.3: Gold-silica coated DNA origami. a) Overview image of a clustered region. b) Close-up image of some of the brighter particles in the clustered region. c) Small gold nuclei on the network background.

At a certain radial distance from the center of the dried in sample droplet, flower shaped particles were observed, see Figure 4.4a and 4.4b. It seems like the drying process separates the particles by size and that the flower shaped structure is a favorable conformation at a certain point in the growth process. The flower shaped particles are smaller than the spherical ones, and therefore considered to be an earlier stage. The bulges could be the consequence of individual growing gold nanoparticles, and this topographic information may be lost as the particles continue to grow. After deposition of a 150 nm thin chromium layer, the topography was preserved at lower magnifications, as in Figure 4.4a. However, finer details were lost. Figure 4.4c shows a particle at high magnification after chromium deposition, and the fine detail topography is due to the quality of the chromium film. This results in a qualitative understanding on how fine details can be expected to be preserved. More images of the flower shaped structures, before and after chromium sputtering, are shown in Appendix A.3.

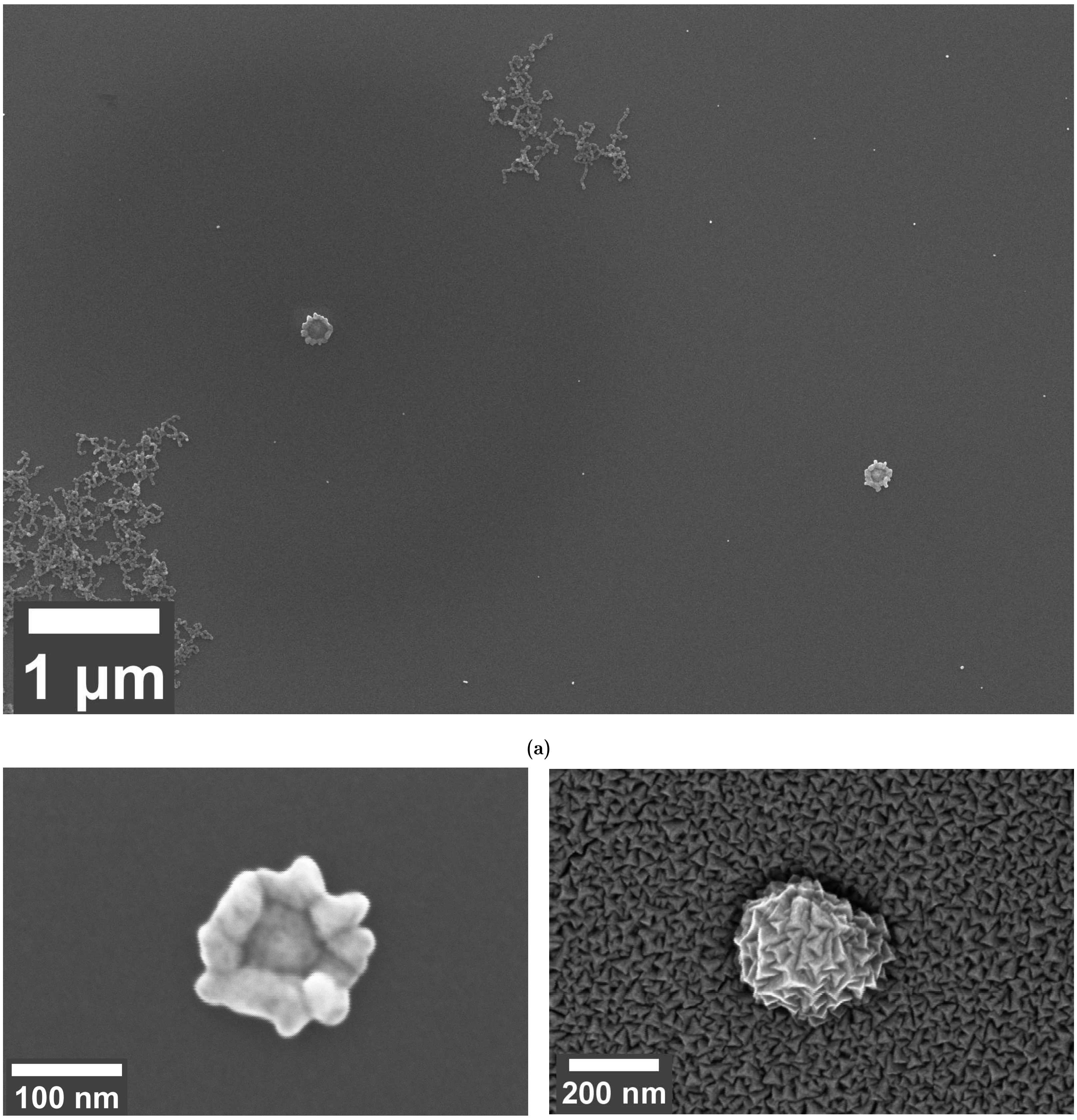

(a)

(b)

(c)

Figure 4.4: Flower shapes particles seen in gold-silica coated DNA origami sample. a) Overview of two particles, showing a common distance between particles. b) Image of a single flower shaped particle. c) Image of a particle of similar size as 4.4b after deposition of 150 nm chromium.

4.3.1 Additional washing step

The same sample was purified a fourth time by centrifuging at 1 500 g for 1 min and washing in H_2O, as an attempt to remove the network structure. After the wash the bright particles remained, and the amount of network background had drastically declined, see Figure 4.5a. As the centrifuge separation was successful, the network structure can be expected to be of lower density than the particles, which also indicates that it is silica gel. Most particles were well separated from other structures as seen in Figure 4.5b, while some were attached to a small piece of network structure, as in 4.5c.

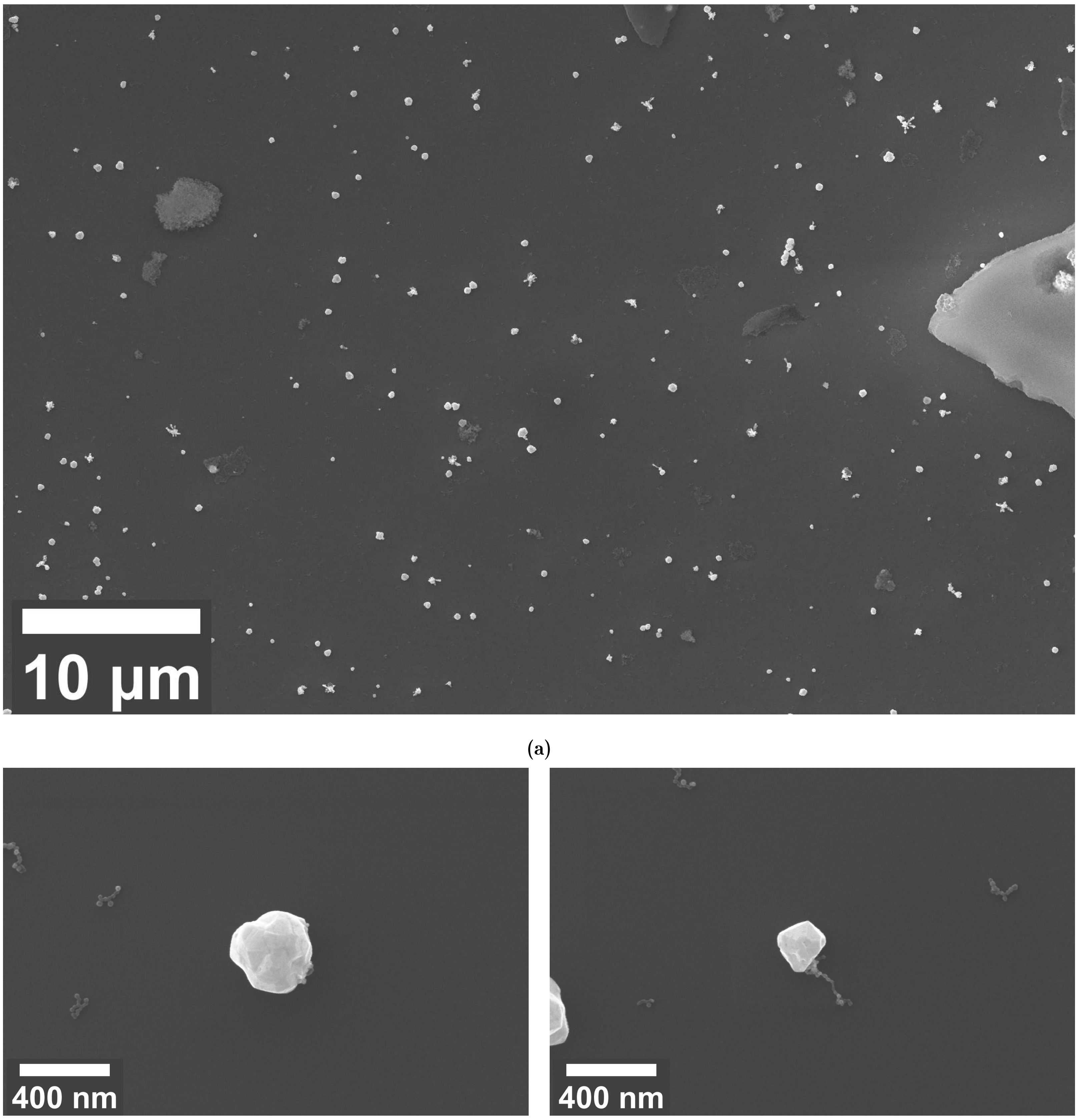

(a)

(b)

(c)

Figure 4.5: Gold-silica coated DNA origami after the fourth washing step. a) Image representative of the entire wafer. b) A particle well separated from other structures. c) A particle attached to a small piece of network structure.

Four EDX measurements were conducted, two on the reoccurring bright particles believed to be gold, one on the reoccurring network believed to be silica gel, and one on a clean part of the wafer as a control. SEM images of the measured positions and EDX spectra are shown in Appendix A.4. The measurements showed that gold is present in the bright particles as expected. However, gold is also present in the structure thought to be silica gel. The silicon signal can always be due to the surrounding or background silicon wafer, so neither the presence nor absence of silica can be determined using this method. Carbon was detected at the particle positions and at the network structure position. The carbon signal does not necessarily confirm that DNA is present, although it is not excluded. Carbon is also present in APTES, which is used as a linker between silica and gold interfaces, and in the citrate ion, used for stabilization of gold particles. The presence of gold around the network structure could be explained as silica gel, slightly coated in gold, as seen in Figure 4.3c.

4.3.1.1 Lift-out

The 100-200 nm thin Au@SiO_2@DNA lift-out contained cross-sections of four particles, see Figure 4.6. The bright region at the bottom of the images is the silicon wafer. The dark spheres are the particles believed to be Au@SiO_2@DNA particles, seen as bright in the previous SEM images. The light gray region surrounding the particles and covering the silicon wafer is the 150 nm thin chromium layer. The darker gray above is the platinum which was deposited in the FIB. The particles are further identified as 1-4 from left to right in Figure 4.6.

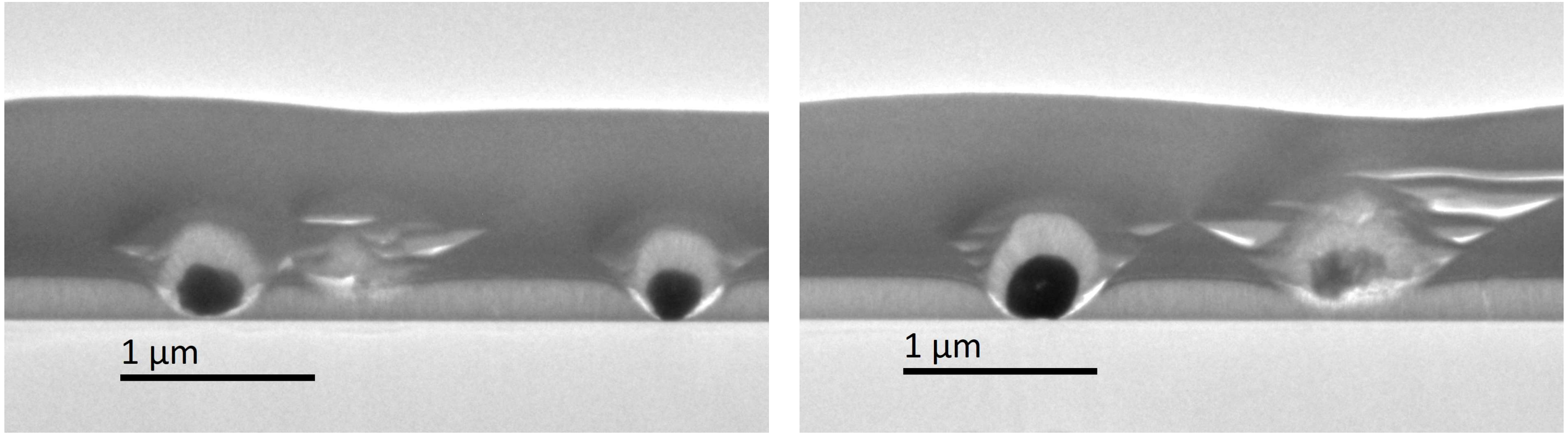

(a)

(b)

Figure 4.6: Overview TEM images of all four particles in the lift-out. The particles are identified as 1-4 from left to right.

The particle diameters before and after the lift-out are shown in Table A.4 in Appendix A.5. The diameter comparison between the top-view SEM image and the cross-section view projection image from TEM was difficult which resulted in low significance of the measurements. What can be said however is that in the lift-out, particle 4 is the most likely to only include the edge of the particle, and particle 3 is the most likely to include the core. That the lift-out only contains the edge of particle 4 is even more evident from the higher brightness of the particle, see Figure

4.6b, as this means that the entire width of the lift-out does not consist of gold and therefore scatter less.

In the center of the projection of particle 3 there is a bright rectangular region, see Figure 4.7a. A solid gold particle would not show this feature, so the center is either hollow or consists of lighter elements. DNA cannot be distinguished based purely on contrast, although, the size of the bright region is comparable to the DNA origami structure seen in plane. In Figure 4.7b a 57x8 nm large rectangle is drawn, corresponding to the size of the pure DNA origami structure seen from a specific direction. The silica coating is then expected to be thin, based on Figure 4.2c, yet still contribute to some size increase in all dimensions. Any tilt would also increase the size of the projection of the DNA origami structure. Since the drawn rectangle is smaller than the bright region, there are many possible orientations that would contribute to such a contrast phenomenon. The lower brightness in the top right corner of the region could also be explained by a SiO_2@DNA core. If a part of the SiO_2@DNA core was etched during the thinning of the lift-out, it is likely to be a corner, leading to a gradient in thickness and therefore also in brightness.

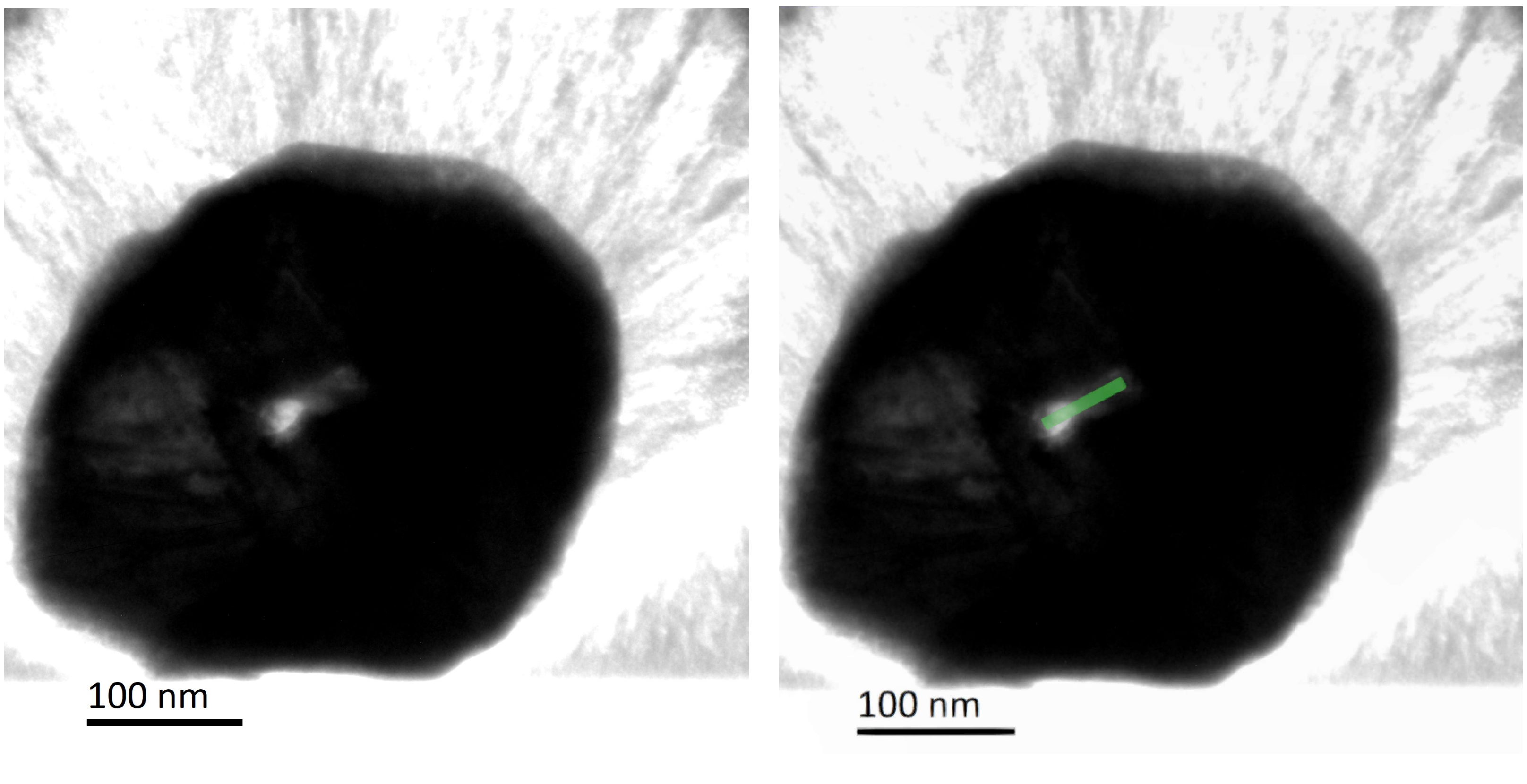

(a) (b)

Figure 4.7: a) Close-up TEM image of particle 3. b) Same as 4.7a except for the addition of a to scale model in green of the DNA origami structure seen in plane.

Particle 2 shows a bright parallelogram, slightly offset from the center, see Figure 4.8a. This could also be the consequence of a SiO_2@DNA core. In Figure 4.8b, a to scale illustration of the DNA origami structure is added, seen from a specific angle. However, the bright spot below the bottom right corner cannot be explained as easily, but could be a consequence of voids in the proximity of the SiO_2@DNA core formed as the gold nanoparticles fuse together. It could also be a corner of another SiO_2@DNA particle within the core, as a consequence of gold shell growth on an aggregate of SiO_2@DNA particles, which would mean that the rest of that

SiO_2@DNA particle should have been etched away during the thinning of the lift-out. The bright spots could also be due to crystallographic defects, however, the contrast would then be expected to be more similar to particle 1, see Figure A.9a.

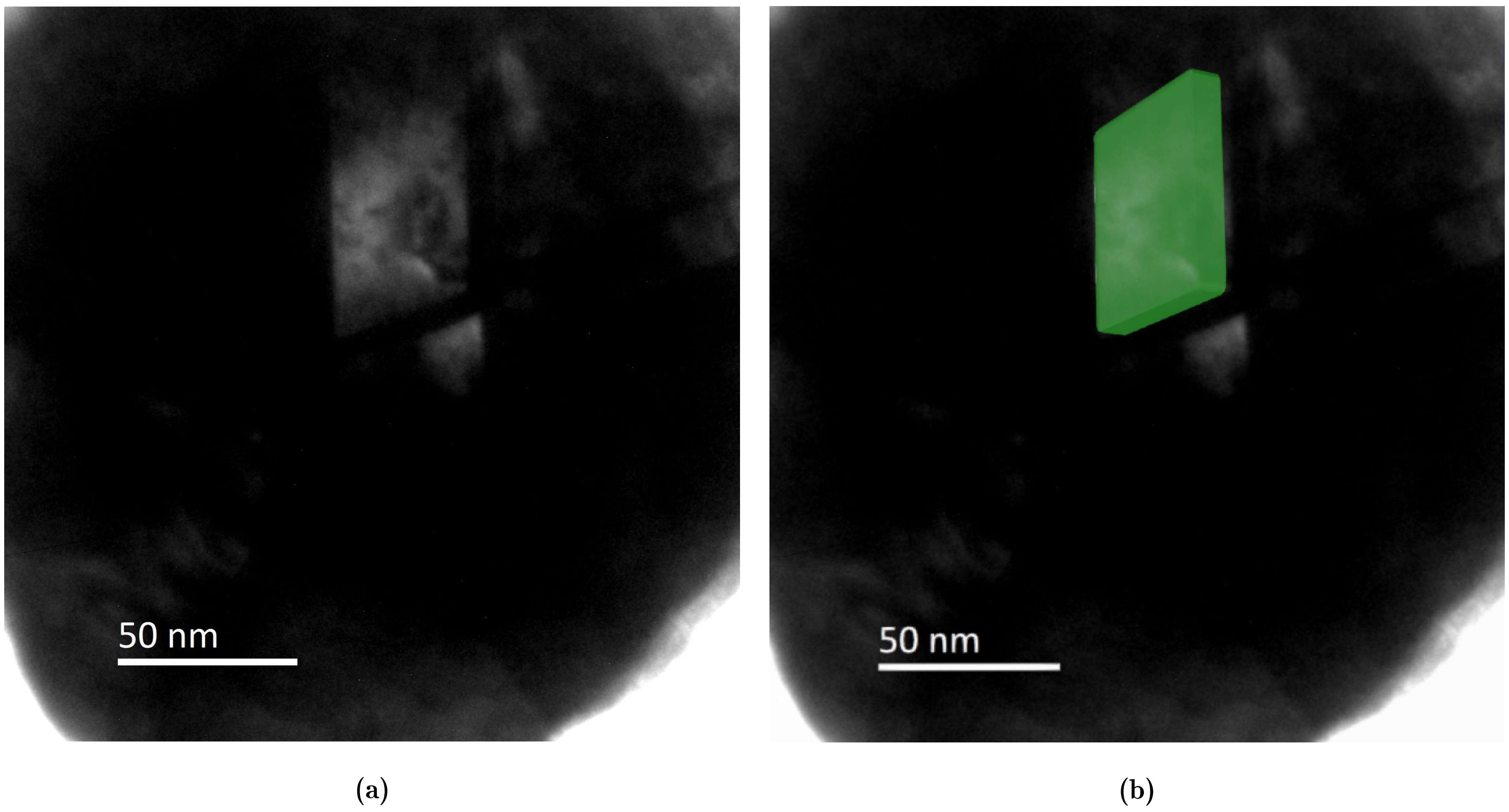

(a) (b)

Figure 4.8: a) Close-up TEM image of particle 2. b) Same as 4.8a except for the addition of a to scale model in green of the DNA origami structure seen from a specific angle.

Neither particle 1 nor 4 showed any contrast features in the center. As particle 4 is a projection of the edge of the particle, it is not expected to include the core and therefore neither any DNA origami. The diameter of particle 1 was the most difficult to measure before the lift-out, as the particle was adjacent to another particle, which is responsible for the defects to the right of particle 1 in Figure 4.6a. The diameter measurements could therefore not be used to evaluate the probability of the projection of particle 1 to include the core. However, since the adjacent particle is not included, the lift-out should include only the edge of particle 1, and thereby no DNA origami. Close-up images of particle 1 and 4 along with an SEM image before the lift-out and a table of all diameters are shown in Appendix A.5.

4.3.2 Gold decrease

The amount of gold was decreased to reduce the particle size, meaning increasing dilution of the gold nanoparticle solution, and decrease of gold hydroxide and formaldehyde. The decrease was performed at a factor 10, 100 and 1000. SEM images are shown in Appendix A.6. The 10x decrease of gold showed an average particle diameter reduction from 395 to 223 nm. At 100x decrease, the network structures remained, but the brighter particles were gone. This indicates that the bright particles are made mainly of gold, yet not excluding that the core is made of SiO_2@DNA, as this size is only slightly larger than 57x52x8 nm.

At 1000x decrease of gold, no structures could be found at all. A decrease of gold should reduce the possibility and size of nucleation sites on a silica gel. The subsequent decrease in density should then reduce the yield during the centrifuge washing procedure. This would explain the complete removal at 1000x decrease of gold, yet still remaining at 100x decrease of gold.

5

Conclusion

The thesis objective was to come further in the research on biomolecule sample preparation for APT 3D analysis. The coating procedures were successful which is an important step to stabilize the structure. SEM images of SiO_2@DNA particles and TEM images of Au@SiO_2@DNA particles showed the expected DNA origami structure, which strongly suggest that the structure is preserved throughout the coating synthesis. The applicability for further 3D structure analysis is therefore considered high.

Various synthesis conditions could be optimized further to increase Au@SiO_2@DNA particle yield, and tailor the particle size. The optimal conditions for DNA origami folding was in 15 mM MgAc based on the obtained yield after purification, which was 55 %. The silica coating methodology produced a thin silica layer of up to a few nanometers as desired, but also an unwanted silica gel. However, the ionic strength might be a reason for the formation of the silica gel, so the concentration of MgAc could therefore be reduced, which in turn also might increase the silica shell thickness. The original gold coating protocol produced a 200 nm gold shell, which is substantially thicker than the silica shell. Scaling down the gold precursor concentrations was proven to decrease the radius. At a tenth of the original concentration, the gold shell became about 110 nm thin instead. An additional washing step of the finished product, by centrifuging at 1 500 g for 1 min and removing the supernatant, showed to greatly reduce the amount of unwanted gel network structure. The 150 nm thin chromium embedding showed a loss of topographic detail, yet sufficient to distinguish the Au@SiO_2@DNA particles.

5.1 Future work

In order to analyze the particles with APT, needle shaped samples with an apex diameter below 100 nm has to be fabricated with the Au@SiO_2@DNA particles at the top. Two suggestions on how to fabricate such tips are explained below.

A similar lift-out as explained in section 3.5.3 could be made on the chromium embedded Au@SiO_2@DNA particle silicon wafer as an initial step. Once the lift-out is ejected with the probe, the end of the lift-out could be welded to a commercially available microtip coupon, which is an array of prefabricated tips which are flat at the apex. The end the lift-out that was attached to the coupon could then be etched loose such that a small lift-out piece remains at the top of the coupon tip. This could then be etched further to obtain a sufficiently thin needle shape, and the center could be adjusted so that it includes a particle.

A more efficient fabrication route, but more uncommon and therefore undetermined, could be to wet etch the silicon wafer with Au@SiO_2@DNA particles on, without any chromium embedding. KOH is a common wet etching chemical which has anisotropic etching properties on silicon, which the wafer is made of, and is weak against both gold and silica, which the particle shells are made of. The anisotropic behavior is usually utilized by adding a mask, often made of silica, on a silicon wafer. Hardly no etching of the silica mask occurs, while the silicon wafer is etched at an angle of 54.74° from the plane at each edge of the mask [35]. Adding a circular dot of silica mask, thereby generates a tip, provided the correct crystallographic orientation of the silicon wafer. The Au@SiO_2@DNA particles may therefore be used as a colloidal mask which should result in tips forming with the particles at the apex. In order to separate the tips, the particle concentration could be reduced prior to surface adsorption. In order to make them sufficiently thin, the particle size could be reduced or a final etching in the FIB could be performed. A potential issue could be the detachment of the Au@SiO_2@DNA particles as the wafer is subjected to the KOH solution. This could perhaps be avoided by increasing the adhesion of the particles to the surface. Examples on how to improve the adhesion could be to surface modify the wafer, for example by adding APTES, or by welding some of the Au@SiO_2@DNA particles to the wafer through platinum deposition in the FIB.

Either process should result in sample tips ready to be analyzed with APT. Laser pulse evaporation would be recommended, as it may be difficult to use electrical pulse evaporation due to the relatively high resistivity of silicon.

Bibliography

[1] *UniParc 2022_01 results*. UniProt. 2022. URL: `https://www.uniprot.org/uniparc/` (visited on 05/17/2022).

[2] *PDB Statistics Overall Growth of Released Structures Per Year*. RCSB PDB. 2022. URL: `https://www.rcsb.org/stats/growth/growth-released-structures` (visited on 05/17/2022).

[3] Marek H. Dominiczak. “Biochemistry and cell biology”. In: *Medical Sciences*. Ed. by Jeannette Naish. 3rd ed. Elsevier, 2019. Chap. 2, pp. 15–56.

[4] Bhasin Manoj and Raghavav G.P.S. “8 - Computational Methods in Genome Research”. In: *Applied Mycology and Biotechnology* 6 (2006), pp. 179–207. DOI: `10.1016/S1874-5334(06)80011-0`.

[5] Ewen Callaway. “Revolutionary cryo-EM is taking over structural biology.” In: *Nature* 578.7794 (2020), p. 201. ISSN: 0028-0836. DOI: `10.1038/d41586-020-00341-9`.

[6] Ewen Callaway. “’It will change everything’: DeepMind’s AI makes gigantic leap in solving protein structures.” In: *Nature* 588.7837 (2020), pp. 203–204. ISSN: 1476-4687. DOI: `10.1038/d41586-020-03348-4`.

[7] Gustav Sundell et al. “Atom Probe Tomography for 3D Structural and Chemical Analysis of Individual Proteins.” In: *Small* 15.24 (2019). ISSN: 1613-6810. DOI: `10.1002/smll.201900316`.

[8] Rukkumani Rajagopalan and Jatinder V. Yakhmi. “Chapter 8 - Nanotechnological approaches toward cancer chemotherapy”. In: *Nanostructures for Cancer Therapy*. Ed. by Anton Ficai and Alexandru Mihai Grumezescu. Micro and Nano Technologies. Elsevier, 2017, pp. 211–240. ISBN: 978-0-323-46144-3. DOI: `10.1016/B978-0-323-46144-3.00008-8`.

[9] Hisashi Tadakuma, Takeya Masubuchi, and Takuya Ueda. “Chapter Five - RNA Study Using DNA Nanotechnology”. In: *Nanotechnology Tools for the Study of RNA*. Ed. by Satoko Yoshizawa. Vol. 139. Progress in Molecular Biology and Translational Science. Academic Press, 2016, pp. 121–163. DOI: `10.1016/bs.pmbts.2015.11.004`.

[10] Swarup Dey et al. “DNA origami.” In: *Nature Reviews Methods Primers* 1.13 (2021). ISSN: 2662-8449. DOI: `10.1038/s43586-020-00009-8`.

[11] Hemangi Ranade and Manali Datta. “Biosensors: Nucleic Acids Sensors; Hybridization Based”. In: *Reference Module in Biomedical Sciences*. Elsevier, 2021. ISBN: 978-0-12-801238-3. DOI: `10.1016/B978-0-12-822548-6.00096-0`.

[12] E. Stahl et al. "Facile and scalable preparation of pure and dense DNA origami solutions." In: *Angewandte Chemie - International Edition* 53.47 (2014), pp. 12735–12740. ISSN: 15213773. DOI: `10.1002/anie.201405991`.

[13] Werner Stöber, Arthur Fink, and Ernst Bohn. "Controlled growth of monodisperse silica spheres in the micron size range". In: *Journal of Colloid and Interface Science* 26.1 (1968), pp. 62–69. ISSN: 0021-9797. DOI: `10.1016/0021-9797(68)90272-5`.

[14] Minh-Kha Nguyen et al. "Ultrathin Silica Coating of DNA Origami Nanostructures." In: *Chemistry of Materials* 32.15 (2020), pp. 6657–6665. ISSN: 08974756. DOI: `10.1021/acs.chemmater.0c02111`.

[15] Tahereh Gholami et al. "Synthesis and characterization of spherical silica nanoparticles by modified Stöber process assisted by organic ligand". In: *Superlattices and Microstructures* 61 (2013), pp. 33–41. ISSN: 0749-6036. DOI: `10.1016/j.spmi.2013.06.004`.

[16] Ralph K. Iler. *Chemistry of Silica - Solubility, Polymerization, Colloid and Surface Properties and Biochemistry.* John Wiley & Sons, 1979. Chap. 3.1 General Theory of Polymerization. ISBN: 978-0-471-02404-0.

[17] S.J Oldenburg et al. "Nanoengineering of optical resonances". In: *Chemical Physics Letters* 288.2 (1998), pp. 243–247. ISSN: 0009-2614. DOI: `10.1016/S0009-2614(98)00277-2`.

[18] Rosa Isela Ruvalcaba Ontiveros et al. "A Simple Way to Produce Gold Nanoshells for Cancer Therapy." In: *http://www.intechopen.com/chapter/pdf-download/64780* (2019). ISSN: 978-1-83881-209-6. DOI: `10.5772/intechopen.82495`.

[19] Hyunho Kang et al. "Stabilization of Silver and Gold Nanoparticles: Preservation and Improvement of Plasmonic Functionalities". In: *Chemical Reviews* 119.1 (2019). PMID: 30346757, pp. 664–699. DOI: `10.1021/acs.chemrev.8b00341`.

[20] Cigdem O. Metin et al. "Stability of aqueous silica nanoparticle dispersions." In: *Journal of Nanoparticle Research: An Interdisciplinary Forum for Nanoscale Science and Technology* 13.2 (2011), p. 839. ISSN: 1388-0764. DOI: `10.1007/s11051-010-0085-1`.

[21] John Turkevich, Peter Cooper Stevenson, and James Hillier. "A study of the nucleation and growth processes in the synthesis of colloidal gold." In: *Discussions of the Faraday Society* 11 (1951), pp. 55–75. ISSN: 03669033. DOI: `10.1039/DF9511100055`.

[22] Magdalena Preciado López et al. "Chapter Seventeen - In Vitro Reconstitution of Dynamic Microtubules Interacting with Actin Filament Networks". In: *Reconstituting the Cytoskeleton.* Ed. by Ronald D. Vale. Vol. 540. Methods in Enzymology. Academic Press, 2014, p. 305. DOI: `10.1016/B978-0-12-397924-7.00017-0`.

[23] Gregory P. Holmes-Hampton, Wing-Hang Tong, and Tracey A. Rouault. "Chapter Fifteen - Biochemical and Biophysical Methods for Studying Mitochondrial Iron Metabolism". In: *Mitochondrial Function.* Ed. by Anne N. Murphy and David C. Chan. Vol. 547. Methods in Enzymology. Academic Press, 2014, pp. 291–292. DOI: `10.1016/B978-0-12-801415-8.00015-1`.

[24] Loren J. Joseph. “Chapter 29 - Setting Up a Laboratory”. In: *Genetic Diagnosis of Endocrine Disorders (Second Edition)*. Ed. by Roy E. Weiss and Samuel Refetoff. Second Edition. San Diego: Academic Press, 2016, pp. 409–426. ISBN: 978-0-12-800892-8. DOI: `10.1016/B978-0-12-800892-8.00029-4`.

[25] Ludwig Reimer. *Scanning Electron Microscopy. [electronic resource] : Physics of Image Formation and Microanalysis*. Springer Series in Optical Sciences: 45. Springer Berlin Heidelberg, 1985, pp. 1–175. ISBN: 9783662135624.

[26] David B. Williams and C. Barry Carter. *Transmission Electron Microscopy. [electronic resource] : A Textbook for Materials Science*. Springer US, 2009, pp. 3–375. ISBN: 9780387765013.

[27] Jae Sung Lee et al. “1.4.5 - Surface Patterning”. In: *Biomaterials Science (Fourth Edition)*. Ed. by William R. Wagner et al. Fourth Edition. Academic Press, 2020, pp. 553–573. ISBN: 978-0-12-816137-1. DOI: `10.1016/B978-0-12-816137-1.00037-4`.

[28] M.Y. Ali and W.N.P. Hung. “1.11 Micromachining”. In: *Comprehensive Materials Finishing*. Ed. by MSJ Hashmi. Oxford: Elsevier, 2017, pp. 322–343. ISBN: 978-0-12-803249-7. DOI: `10.1016/B978-0-12-803581-8.09156-6`.

[29] J. Orloff. “Focused Ion Beam Characterization Techniques”. In: *Reference Module in Materials Science and Materials Engineering*. Elsevier, 2016. ISBN: 978-0-12-803581-8. DOI: `10.1016/B978-0-12-803581-8.03523-2`.

[30] Baptiste Gault et al. “Atom probe tomography”. In: *Nature Reviews Methods Primers* 1.1 (July 2021), p. 51. ISSN: 2662-8449. DOI: `10.1038/s43586-021-00047-w`.

[31] Charlie Kong, Soshan Cheong, and Richard D. Tilley. “2.15 - Recent Development in Focused Ion Beam Nanofabrication”. In: *Comprehensive Nanoscience and Nanotechnology (Second Edition)*. Ed. by David L. Andrews, Robert H. Lipson, and Thomas Nann. Second Edition. Oxford: Academic Press, 2019, pp. 327–356. ISBN: 978-0-12-812296-9. DOI: `10.1016/B978-0-12-803581-8.10432-1`.

[32] S. Lozano-perez. “13 - Characterization techniques for assessing irradiated and ageing materials in nuclear power plant systems, structures and components (SSC)”. In: *Understanding and Mitigating Ageing in Nuclear Power Plants*. Ed. by Philip G. Tipping. Woodhead Publishing Series in Energy. Woodhead Publishing, 2010, pp. 389–416. ISBN: 978-1-84569-511-8. DOI: `10.1533/9781845699956.3.389`.

[33] W. Chen and P. Pareige. “11 - Using atom probe tomography in the study of semiconductor nanowires”. In: *Semiconductor Nanowires*. Ed. by Jordi Arbiol and Qihua Xiong. Woodhead Publishing Series in Electronic and Optical Materials. Woodhead Publishing, 2015, pp. 305–326. ISBN: 978-1-78242-253-2. DOI: `10.1016/B978-1-78242-253-2.00011-6`.

[34] Baptiste Gault et al. *Atom Probe Microscopy. [electronic resource]*. Springer Series in Materials Science: 160. Springer New York, 2012. ISBN: 9781461434368.

[35] *KOH ETCHING*. Brigham Young University. 2022. URL: `https://cleanroom.byu.edu/koh` (visited on 05/31/2022).

[36] *DNA and RNA Molecular Weights and Conversions*. ThermoFisher Scientific. 2022. URL: `https://tinyurl.com/mpfxhj2b` (visited on 05/26/2022).

A

Appendix 1

A.1 DNA origami folding buffers

Six folding reactions with different folding solvents were conducted. The solvents and corresponding sample IDs are shown in Table A.1. The obtained UV/Vis spectra of the six reactions before and after thermal annealing are shown in Figure A.1a and A.1b respectively. Five out of the six reaction protocols showed similar curves and were therefore assumed to be correctly folded. Three of the mentioned samples were PEG purified, and the following UV/Vis measurements showed the highest DNA concentration in protocol 3 corresponding to 15 mM MgAc as solvent, see Figure A.1c. The concentration was 50.8 ng/µl, corresponding to 10.9 nM, based the molecular weight of 4 649 632 Da. The molecular weight was calculated based on the known sequence, and the molecular weight of each nucleotide [36], and is presented in Table A.2.

Table A.1: Folding buffers used during the DNA origami folding reactions, in addition to what the pure staple and scaffold DNA strands were dissolved in.

Sample ID	Solvent
1	40 mM tris, 20 mM acetic acid, 1 mM EDTA, 15 mM MgAc
2	40 mM tris, 20 mM acetic acid, 1 mM EDTA
3	15 mM MgAc
4	10 mM tris, 1 mM EDTA
5	10 mM tris, 1 mM EDTA, 15 mM MgAc
6	None

Table A.2: Data required for calculations leading up to the total molar mass of one DNA origami structure: 4 649 632 Da.

	Adenine	Thymine	Guanine	Cytosine
Number of bases	4169	4777	3057	3058
Base mass (Da)	313,2	304,2	329,2	289,2
Total mass (Da)	1 305 730,8	1 453 163,4	1 006 364,4	884 373,6

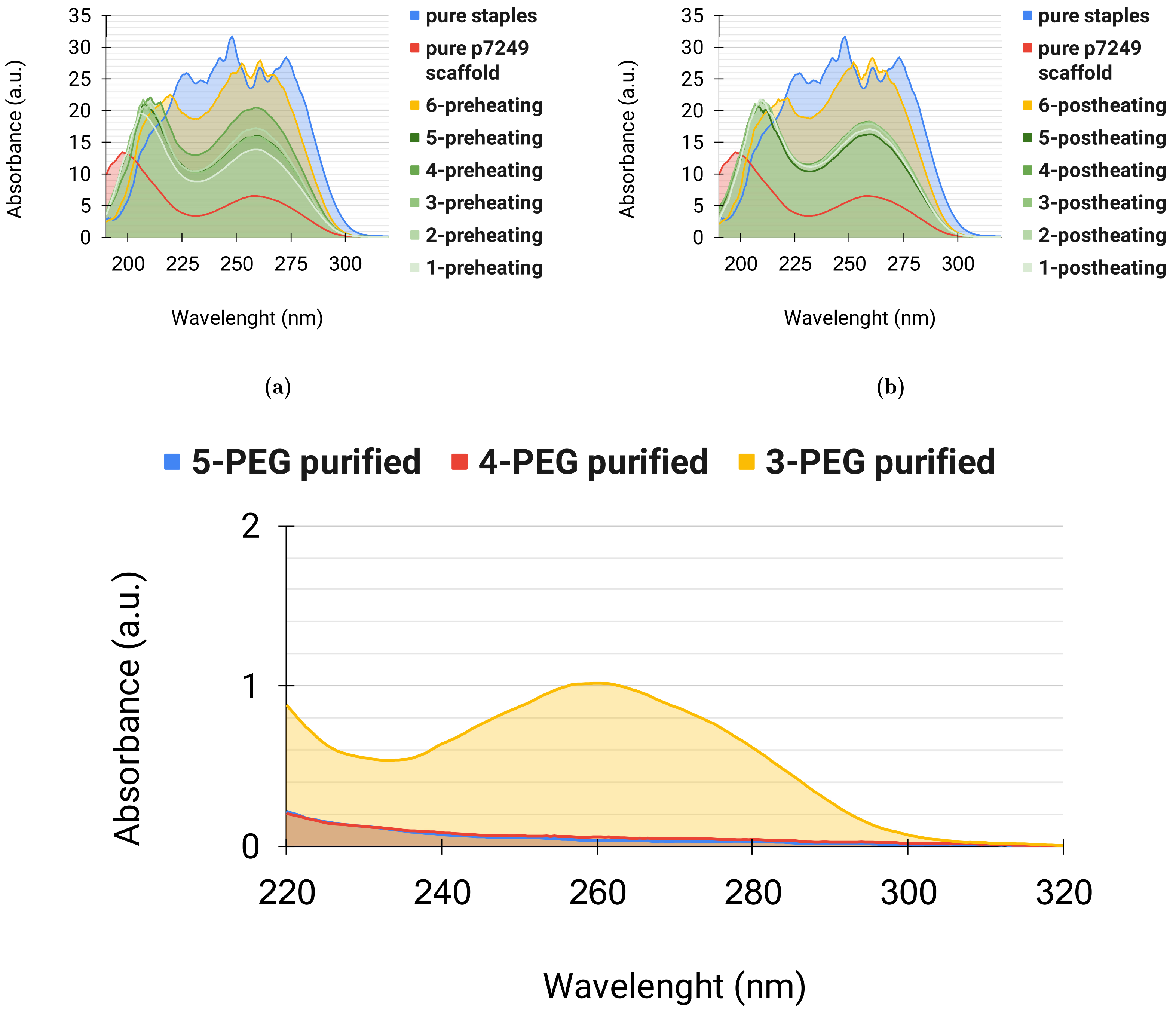

(a)

(b)

(c)

Figure A.1: UV/Vis spectra of DNA origami folded in different solvents, see Table A.1 for description of sample index. a) All 6 mixtures before thermal annealing and the pure staple and scaffold DNA. a) All 6 mixtures after thermal annealing and the pure staple and scaffold DNA. c) 3 of the mixtures after PEG purification.

A.2 DNA concentration after silica coatings

After the primary coating a DNA concentration of 0.8 nM was measured for sample 3, see Table A.1. The corresponding UV/Vis spectrum can be seen in Figure A.2a. The UV/Vis spectrum has a different shape than before, most likely due to the silica shell, meaning that the precision of the measure value could be considered lower. After the secondary coating no DNA could be measured, most likely due to dilution of the sample prior to the secondary coating synthesis. The corresponding UV/Vis spectrum can be seen in Figure A.2b.

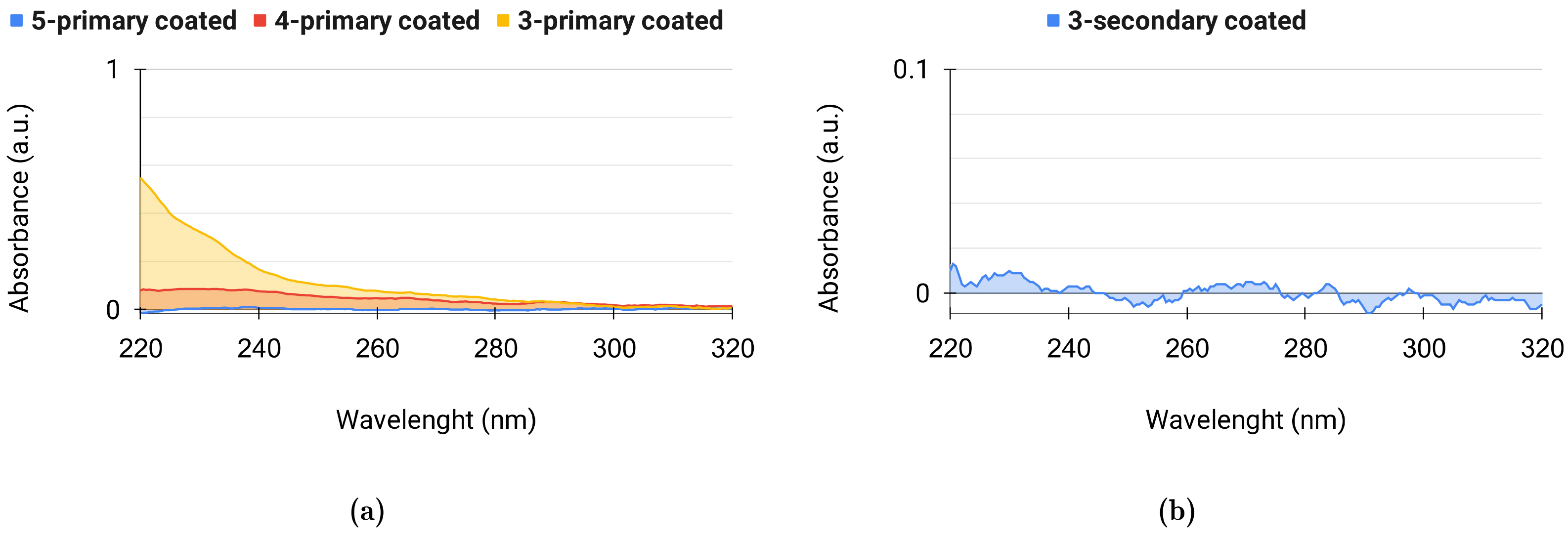

Figure A.2: UV/Vis spectra of DNA origami coated in silica. Sample index described in Table A.1. a) Spectra after primary coating and purification. b) Spectrum after secondary coating and purification.

A.3 Flower shaped particles

A smaller droplet of 5 µl was used to dry in the sample, which did not cover the entire wafer. A gradient of particle concentration was therefore observed at the edge of the droplet position. At a certain radial position close to the edge of the sample drying ring, flower shaped particles were seen. Overview images where it can be seen how densely packed the structures were can be seen in Figure A.3, and close up images of the structures can be seen in Figure A.4.

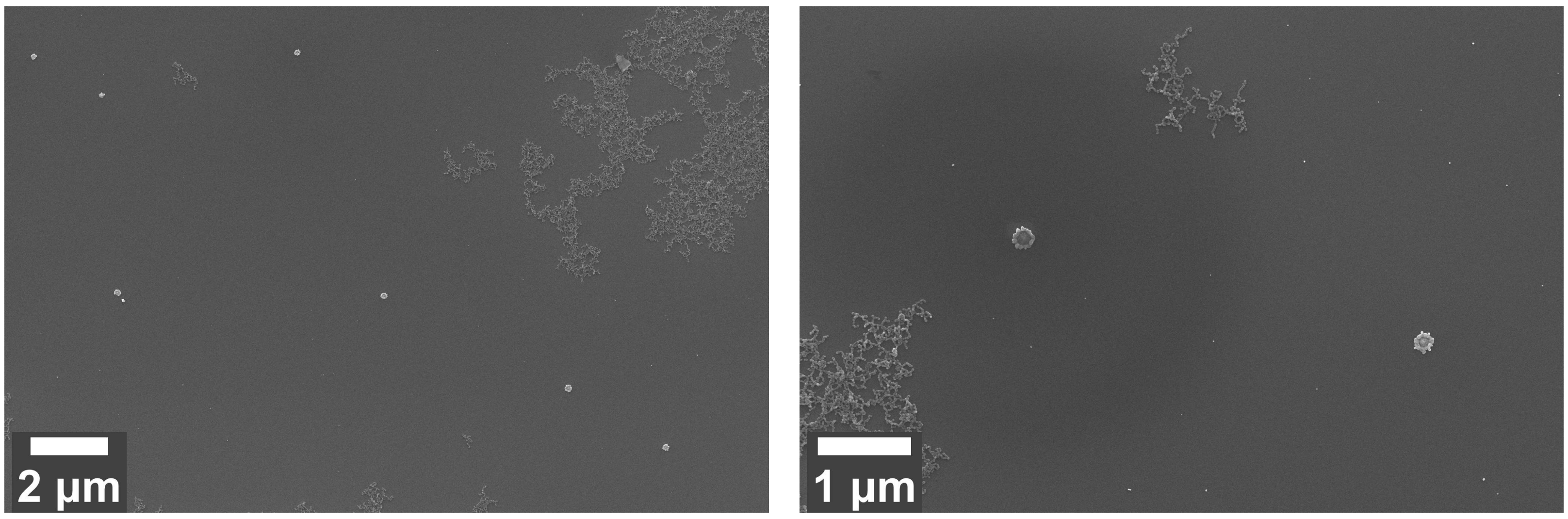

Figure A.3: Overview images were several flower shaped structures can be seen.

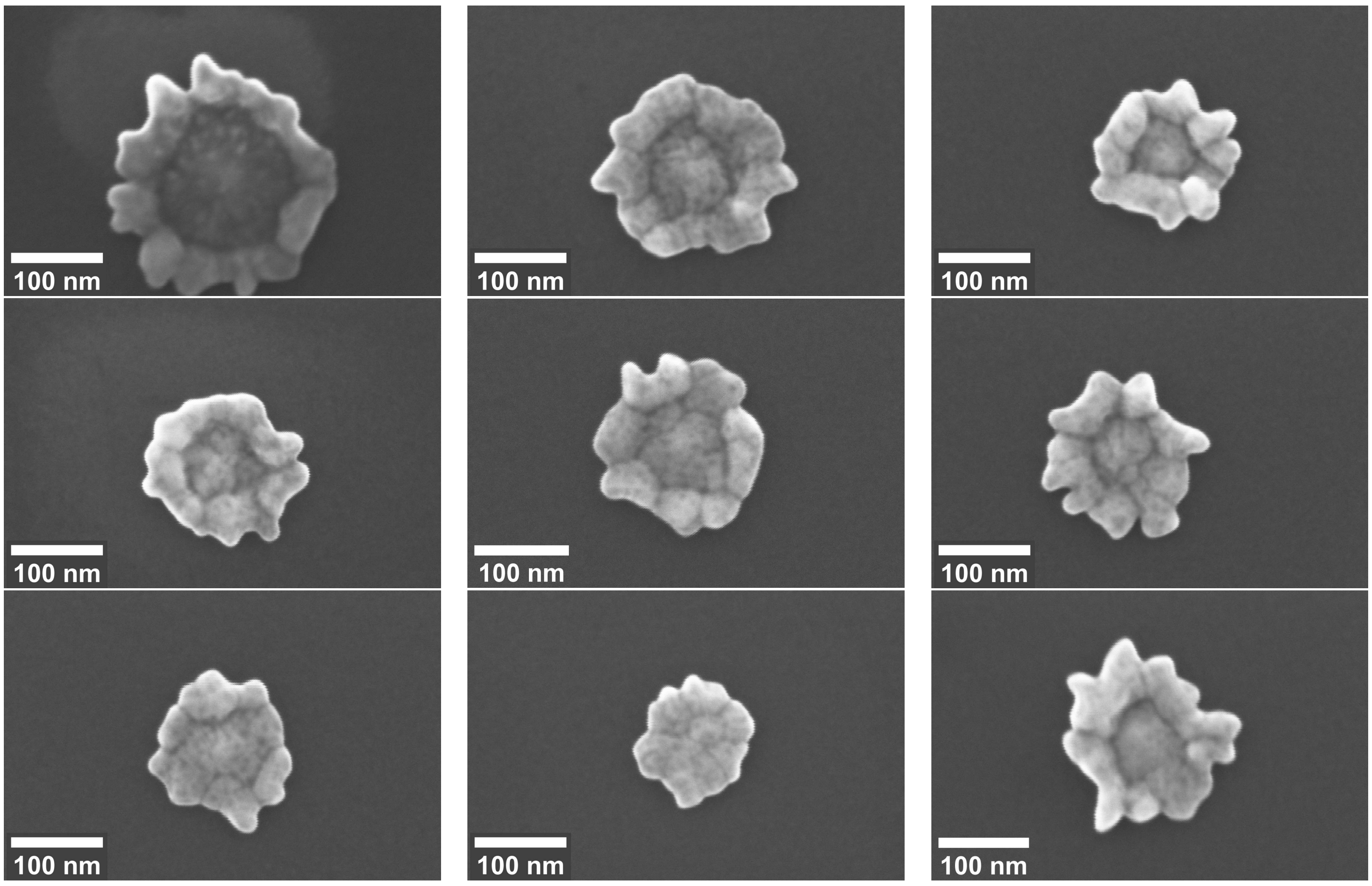

Figure A.4: Close up images of flower shaped particles. All images have the same scale bar sizes.

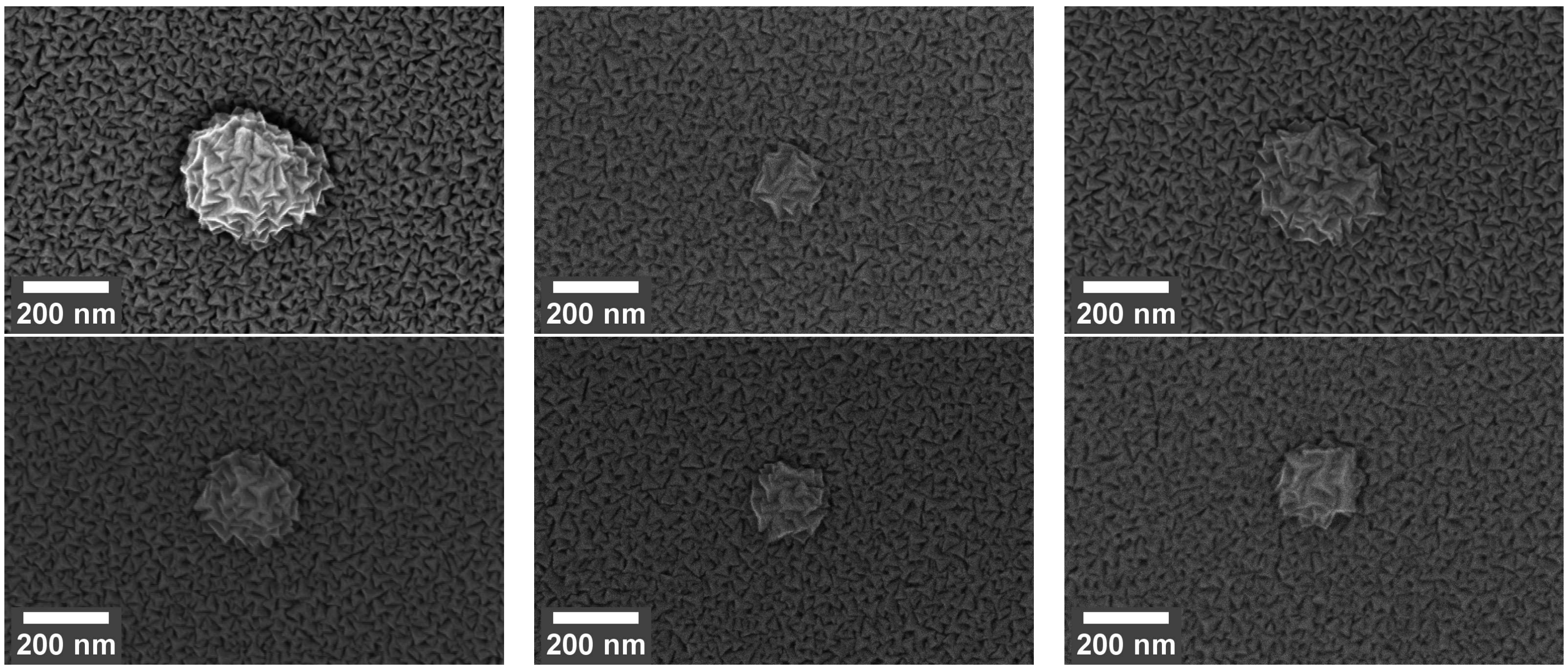

Figure A.5: Close up images of particles after 150 nm of chromium sputtering. All images have the same scale bar sizes. The increased brightness of the top left particle is due to more properly tuned imaging parameters in the SEM, and not due to the particle itself.

A.4 EDX measurements

Four spectra were obtained, two from the reoccurring bright particles believed to be gold, one from the reoccurring network believed to be silica gel, and one from pure wafer as a control, see Figure A.6.

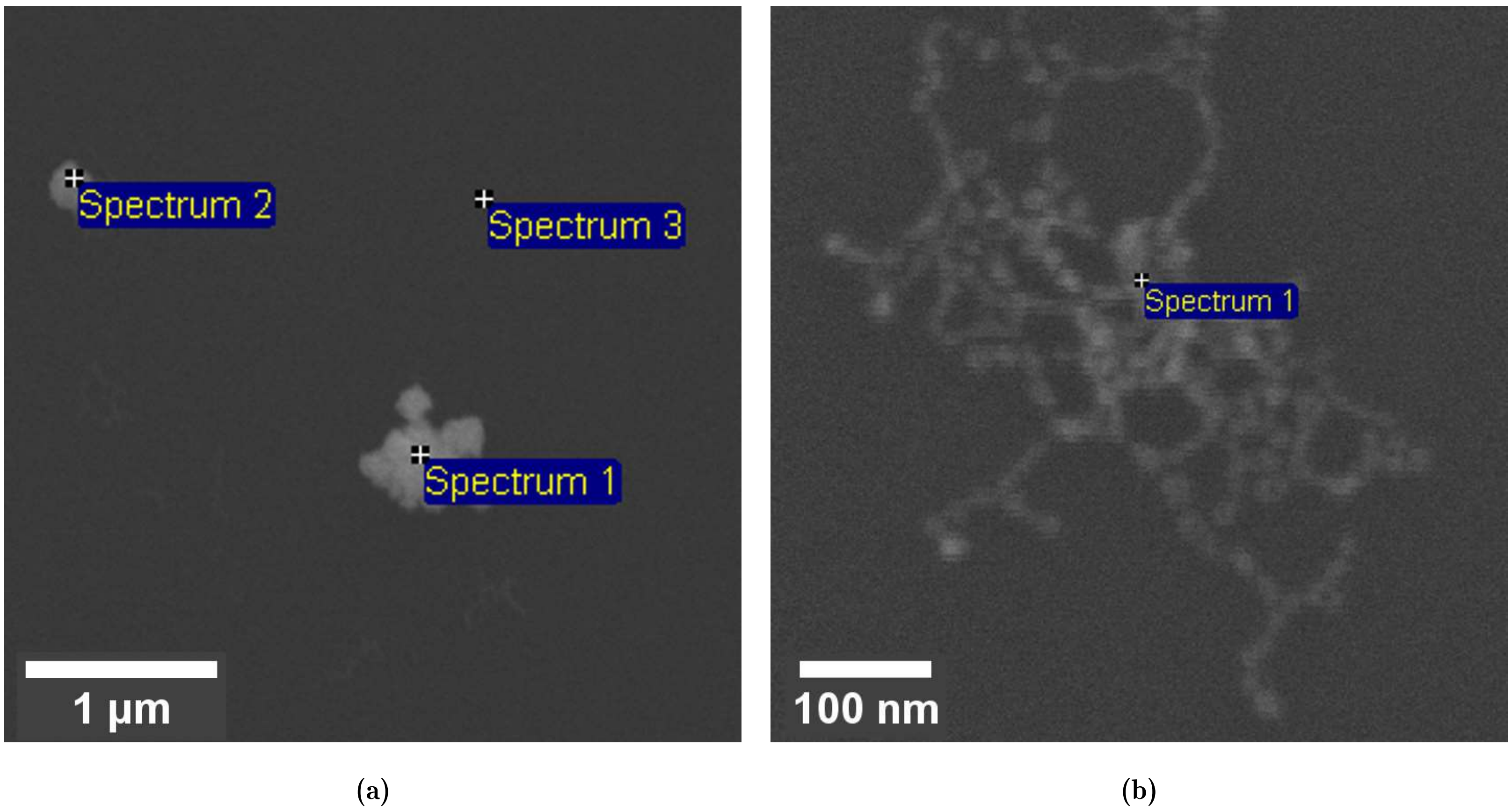

(a) (b)

Figure A.6: SEM images with markings where EDX measurements were performed. a) Spectrum 1, 2 and 3 corresponds to position 1, 2 and 3 respectively. Position 1 and 2 are on bright particles, and position 3 on pure wafer. b) Spectrum 1 corresponds to position 4 further on. Position 4 is on one of the network structures previously believed to be a silica gel network.

The obtained data is both summarized in Table A.3, and in Figure A.7. Be aware of that the tabular values are more approximated than what they seem. The investigated volume of EDX measurements is larger than that of secondary electrons, which form the images in Figure A.6, meaning that the background wafer also can contribute to the signal, especially at position 4 where the particles are smaller. The reliability also decreases for lighter elements, such as carbon and fluorine.

Table A.3: EDX measurements in the positions shown in Figure A.6, shown by weight and atomic percentage. The precision of the values is low, and light elements are less reliable.

Element	**Position 1**		**Position 2**		**Position 3**		**Position 4**	
	wt. %	***at. %***	***wt. %***	***at. %***	***wt. %***	***at. %***	***wt. %***	***at. %***
Si	24.39	49.77	65.12	80.13	100.00	100.00	85.43	81.15
Au	68.55	19.95	29.80	5.23	-	-	6.48	0.88
C	5.11	24.38	5.09	14.64	-	-	8.09	17.97
F	1.96	5.90	-	-	-	-	-	-

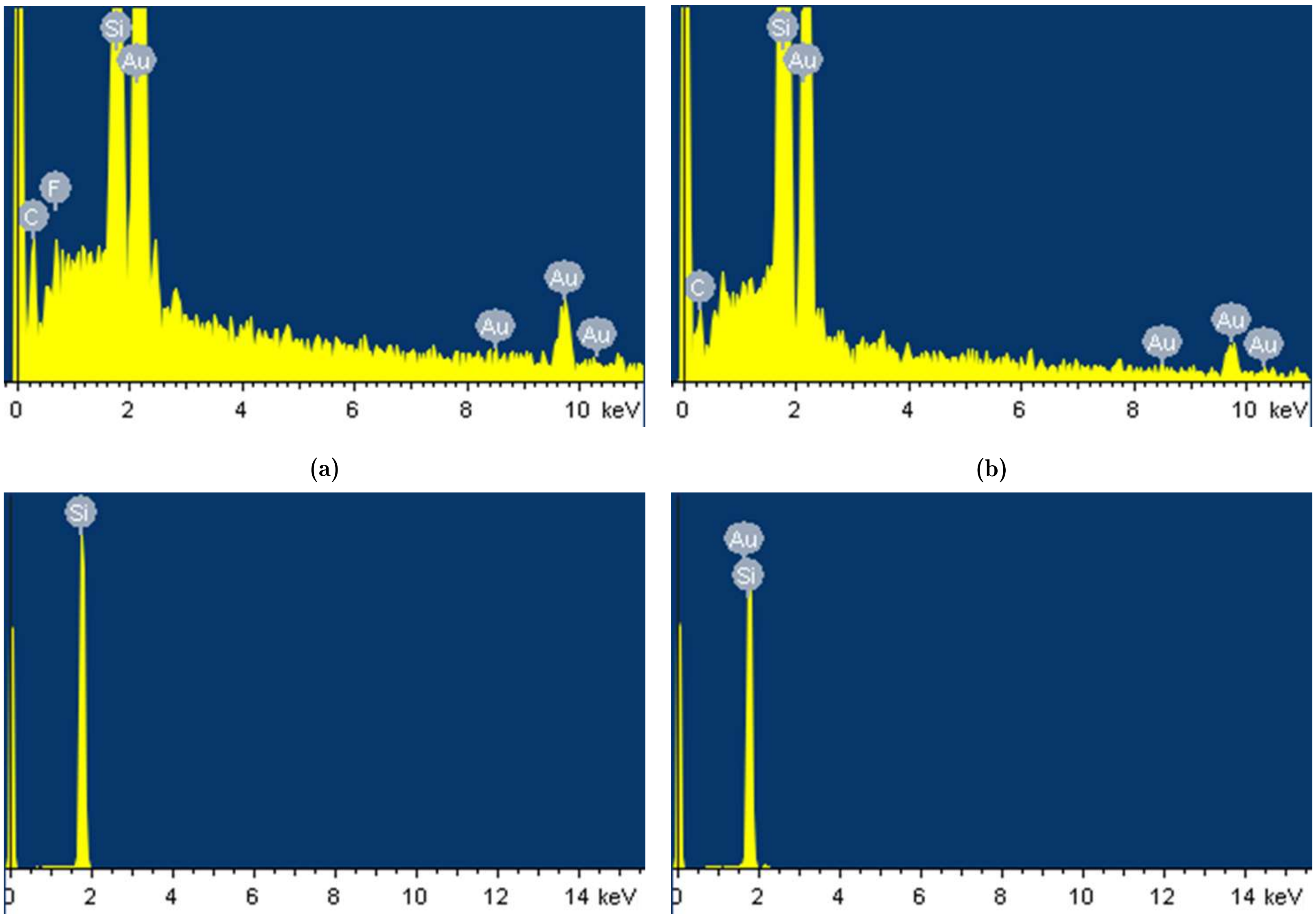

(a)

(b)

(c)

(d)

Figure A.7: EDX spectra. a) Position 1. b) Position 2. c) Position 3. d) Position 4.

A.5 TEM images and measurements

The measured diameters of each particle are shown in Table A.4. The initial diameters were measured along the direction of the long side of the deposited platinum in the image shown in Figure A.8, and the cross-section diameters in the image shown in Figure 4.6. As it was unclear, in the TEM images in Figure 4.6, where the variation in topography was high enough to result in distinct contrast difference in the SEM image, a minimum and maximum diameter was measured. The SEM image shows the particle size after chromium coverage, and it is therefore the size of the chromium topographic disruption that should be measured in the TEM images to be able to compare, and not the actual particle. The distance between the core of the particle, and the part of the lift-out closest to the core, was then approximated using the formula shown in Equation A.1. The equation is derived through basic trigonometry and spherical particle approximation. D_{core} corresponds to the core lift-out distance, $\varnothing_{Initial}$ to the initial diameter, and $\varnothing_{Lift-out}$ to the diameter measured in the TEM. The average value, using the minimum and the maximum cross-section diameter, is also presented in Table A.4. Note that the maximum cross-section diameter is larger than the initial for particle 3, resulting in Equation A.1 being undefined, and $D_{core} = 0$ was therefore used for that specific measurement since the core is expected to be within the lift-out. Additional TEM images of particle 1 and 4 are also shown in Figure A.9.

$$D_{core} = \frac{\sqrt{\varnothing^2_{Initial} - \varnothing^2_{Lift-out}}}{2} \tag{A.1}$$

Table A.4: Measured diameters of the particles in the lift-out, prior to the lift-out and afterwards. The diameters from the TEM cross-section images, after the lift-out, are divided in minimum and maximum values. The distance from the core is based on a spherical approximation of the particle.

Particle ID	**Diameters (nm)**			**Average distance from the core (nm)**
	Initial	**Minimum cross-section**	**Maximum cross-section**	
1	963	526	861	309
2	875	480	745	298
3	893	583	1006	169
4	1152	563	1114	325

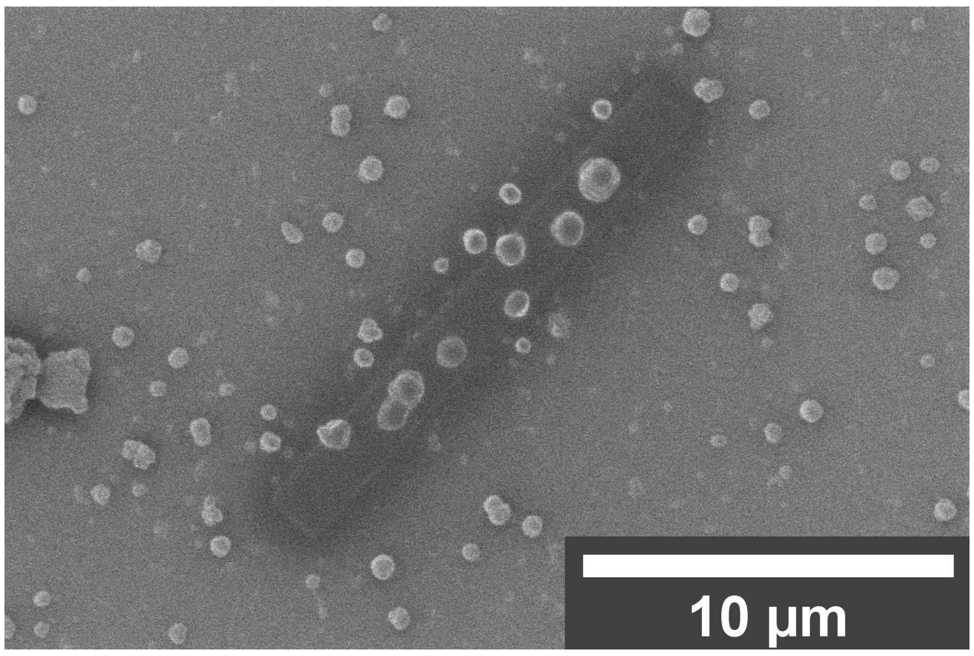

Figure A.8: SEM image in the FIB seconds after initiation of platinum deposition on a 15x1.5 µm area, which is the lift-out area. The later thinning of the lift-out resulted in that only about 100 nm of the 1 500 nm width was included.

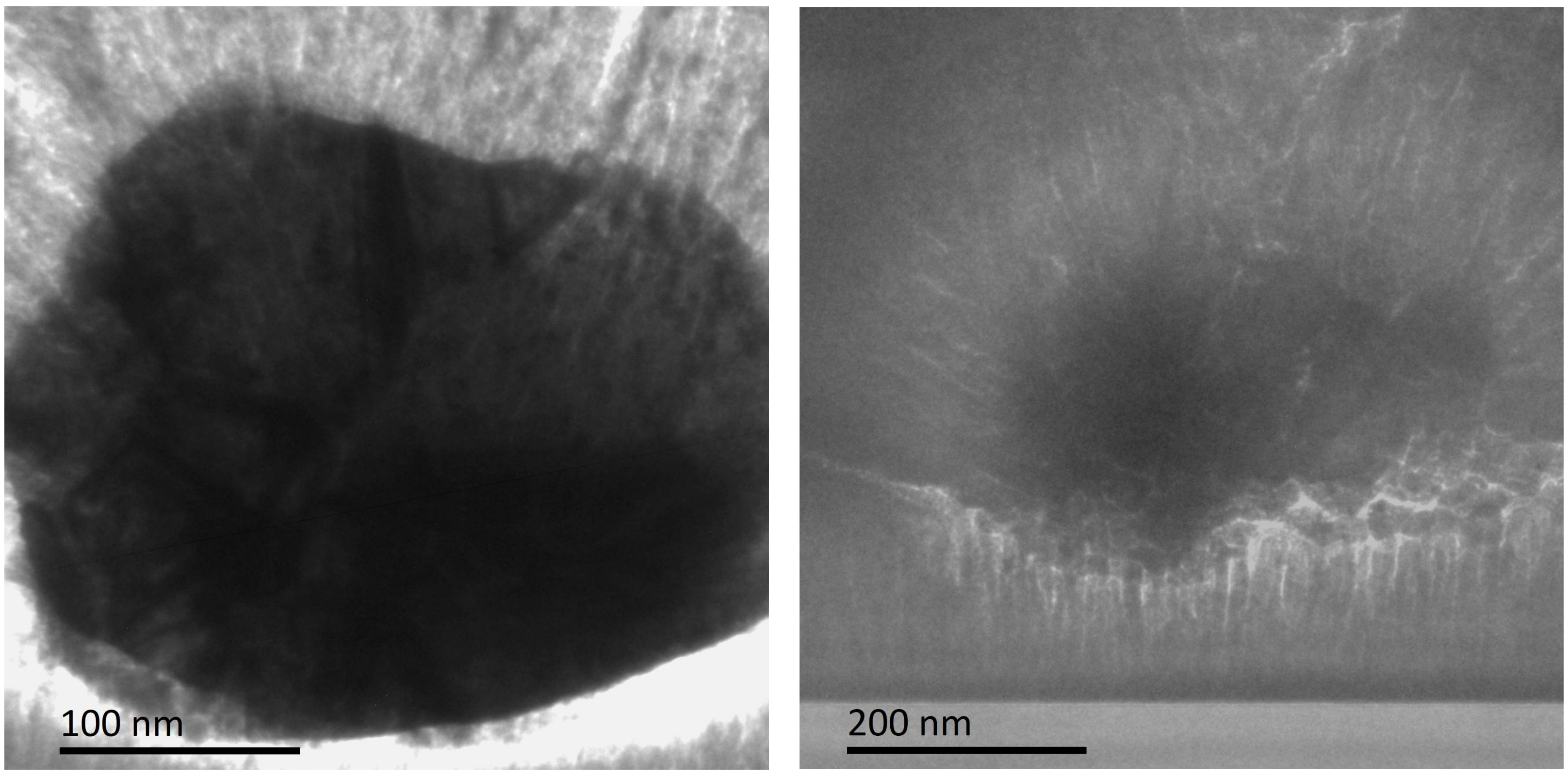

(a) (b)

Figure A.9: Close-up TEM images of Au@SiO$_2$@DNA particles in cross-section. Neither projections are expected to contain the center of the particles, and therefore DNA origami, and no contrast variations occur in the center of the projection. a) Particle 1. b) Particle 4.

A.6 Gold decrease images

A comparison between the particle sizes in the original concentration of gold and in the 10x decrease of gold is shown in Table A.5. Overview images of 10x and 100x decrease of gold samples are shown in Figure A.10a and A.10c respectively. A close up image of a particle on the 10x decrease of gold surface is shown in Figure A.10b.

Table A.5: Sizes of brighter particles found on the surfaces with 1x and 1/10x gold concentration.

Sample	Diameter (nm)	Measurements	
		Particles	***Total***
1x gold	395 ± 22	19	152
1/10x gold	223 ± 35	2	16

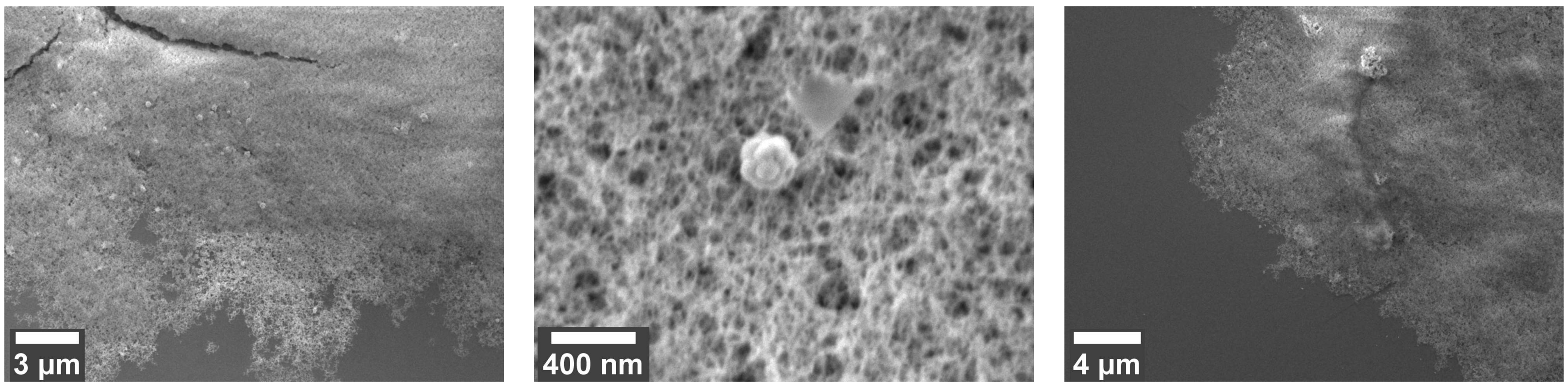

(a) (b) (c)

Figure A.10: SEM images of surfaces with samples containing a reduced amount of gold. a) An overview image of the surface with 10x decrease of gold. b) One particle at the surface with 10x decrease of gold. c) An overview image of the surface with 100x decrease of gold.

DEPARTMENT OF CHEMISTRY AND CHEMICAL ENGINEERING
CHALMERS UNIVERSITY OF TECHNOLOGY
Gothenburg, Sweden
www.chalmers.se

CHALMERS
UNIVERSITY OF TECHNOLOGY